

DEVELOPMENT OF SILVER NANOPARTICLE DECORATED ZnO NANOROD ARRAY-BASED HIGHLY SENSITIVE AND FLEXIBLE UV- PHOTODETECTOR

MS (Research) Thesis

By

NEERAJ NIKHIL



**DEPARTMENT OF ELECTRICAL ENGINEERING
INDIAN INSTITUTE OF TECHNOLOGY INDORE**

JULY 2025

DEVELOPMENT OF SILVER NANOPARTICLES DECORATED ZnO NANOROD ARRAY-BASED HIGHLY SENSITIVE AND FLEXIBLE UV- PHOTODETECTOR

A THESIS

*Submitted in fulfillment of the
requirements for the award of the degree
of*

Master of Science (Research)

by

NEERAJ NIKHIL



**DEPARTMENT OF ELECTRICAL ENGINEERING
INDIAN INSTITUTE OF TECHNOLOGY INDORE**

JULY 2025



INDIAN INSTITUTE OF TECHNOLOGY INDORE

CANDIDATE'S DECLARATION

I hereby certify that the work which is being presented in the thesis entitled **DEVELOPMENT OF SILVER NANOPARTICLE DECORATED ZnO NANOROD ARRAY-BASED HIGHLY SENSITIVE AND FLEXIBLE UV-PHOTODETECTOR** in the fulfillment of the requirements for the award of the degree of **MASTER OF SCIENCE (RESEARCH)** and submitted in the **DEPARTMENT OF ELECTRICAL ENGINEERING, Indian Institute of Technology Indore**, is an authentic record of my own work carried out during the time period from July 2022 to July 2025 under the supervision of Prof. Vipul Singh, Indian Institute of Technology Indore.

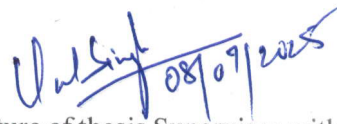
The matter presented in this thesis has not been submitted by me for the award of any other degree of this or any other institute.


8.07.2025

Signature of the student with date

NEERAJ NIKHIL

This is to certify that the above statement made by the candidate is correct to the best of my
/our knowledge.


08/07/2025

Signature of thesis Supervisor with date


(Prof. Vipul Singh)

NEERAJ NIKHIL has successfully given his/her MS (Research) Oral Examination held 03-07-2025.

Signature of Chairperson (OEB) with date


08/07/2025
Signature(s) of Thesis Supervisor(s) with date


09/07/25
Signature of Convener, DPGC with date


09.07.2025
Signature of Head of Discipline with date

ACKNOWLEDGEMENTS

I would like to express my profound appreciation to **Prof. Vipul Singh**, my esteemed supervisor at IIT Indore, whose exceptional mentorship has been a cornerstone of my research. His passion for scientific exploration and his unwavering commitment to excellence have been a constant source of motivation. His thoughtful guidance and insightful suggestions have significantly shaped both my research and personal growth. I am forever indebted to him for his invaluable support, which has been instrumental in helping me navigate and present my work with clarity and precision. I want to extend my sincere gratitude to my PSPC members, **Dr. Amod C. Umarikar** (Associate Professor, Discipline of Electrical Engineering, IIT Indore) and **Dr. Onkar Game** (Assistant Professor, Discipline of Physics, IIT Indore), for their insightful observations and valuable feedback. Their expertise and constructive criticism have significantly contributed to refining the quality of my research work.

I am extremely grateful to my colleagues from the **Molecular and Nanoelectronics Research Group (MNRG)**—**Dr. Jitesh Agrawal**, **Dr. Tejswini K. Lahane**, **Ms. Sidhi G. Ramer**, **Ms. Navneet Chauhan**, **Mr. Anand Kachale**, **Mr. Puranjeet Pahari**, **Ms. Ashreta Sahay**, **Mr. Atharv Limaye**, **Mr. Bhawesh Chandraker**, **Mr. Rushikesh hake**, and **Mr. Nisarg Purabiarao**—for their assistance and motivation during the experimental work. Our discussions and collective efforts in the lab have broadened my understanding and deepened my expertise in the field. My heartfelt thanks go to my loving parents, **Shri. Tripurari Prasad** and **Smt. Nita Sinha**, and my brothers, **Mr. Rahul Kumar** and **Mr. Sonu Raj**. Their immeasurable sacrifices, boundless encouragement, and steadfast belief in my abilities have been my greatest pillars of strength. achievement would not have been possible.

I am also deeply indebted to my friends, **Radheshyam Sharma, Sai Ganesh, Gulrez Khan Lodi, Ankit Patel, Shruti Ghodke, and Komal Gupta**, for their continuous motivation and unwavering belief in my potential. Their friendship has made this experience all the more meaningful and joyful.

My thanks are also due to **Mr. Atul Singh** and **Mr. Nitin Upadhyay** from **SIC IIT Indore** for their technical assistance and cooperation throughout my research during my academic tenure.

I would also like to acknowledge the **Ministry of Human Resource Development (MHRD)** for the financial assistance that made this research possible. Their support allowed me to focus wholeheartedly on my work. Our sincere thanks to Dr. Suhas Joshi, The Director of IIT Indore for his unwavering support and encouragement.

Lastly, I extend my gratitude to all those—both known and unknown—who have contributed, directly or indirectly, to the successful completion of my thesis. Your contributions, no matter how small, have left a lasting impact on this work.

To each of you, I offer my deepest thanks and sincere appreciation.

Dedicated
to
my family and friends

Abstract

ZnO-based UV photodetectors are highly desired for various applications, viz., wearable dosimeter, biomedical, defense, and communications. This work reports a ZnO-based photoconductive device with inter-digitated planar silver electrodes deposited over ZnO nanorod array (NRA), capped with silver nanoparticles. The FESEM image confirmed the growth of ZnO NRA. The photosensitive devices thus developed were found to be stable in air, showing high photosensitivity of 4.2×10^7 , against a $\lambda=330$ nm UV light illumination, demonstrating a high UV-Vis rejection ratio. The ZnO nanorod array (NRA) was deposited via the hydrothermal technique over functionalized and precleaned polyimide substrates. These substrates were then capped with silver nanoparticles (Ag-NPs) using the photochemical reduction technique. ZnO NRA capped with Ag-NPs demonstrated improved photosensitivity and responsivity, compared to the devices developed using pristine ZnO, especially for small-sized silver nanoparticles. These observations were corroborated to the plasmonic coupling between Ag-NPs and ZnO NRs. The intensity of light was maintained at 0.8 mW/cm^2 . Additionally, these devices were developed on the polyimide substrate, hence they were flexible and could sustain multiple bending cycles (~ 100) without showing any significant degradation in their performance. This work demonstrated the potential of effective plasmonic coupling between Ag-NPs and ZnO NRs and its effective utilization towards the development of highly sensitive UV photodetectors, and also highlights the potential of this effective solution-processed-based technique in the development of highly sensitive, air-stable, flexible UV photodetectors.

Table of Contents

List of Figure	ix
-----------------------	-----------

List of Tables	xi
-----------------------	-----------

List of Nomenclature and Acronyms	xii
--	------------

1. Introduction.....	1
-----------------------------	----------

1.1 Photodetector:.....	1
-------------------------	---

1.1.1 Types of photodetectors:	1
--------------------------------------	---

1.2 ZnO.....	4
--------------	---

1.2.1 Structural Properties.....	4
----------------------------------	---

1.2.2 Optoelectronic properties	6
---------------------------------------	---

1.2.3 ZnO Nanostructures	6
--------------------------------	---

1.2.4 Synthesis of ZnO nanostructure:	7
---	---

1.2.5 Working of ZnO nanostructured-based UV	11
---	----

1.3 LSPR (localized surface plasmon resonance)	13
--	----

1.3.1 Applications of Nanoplasmonics:	16
---	----

1.4 Challenges:	16
-----------------------	----

1.5 Review of past work:.....	18
-------------------------------	----

1.5.1 Objectives of this work	20
-------------------------------------	----

1.6 Organization of Thesis	19
----------------------------------	----

2. Experimental Procedure and Characterization

Techniques	27
-------------------------	-----------

2.1 Introduction	27
------------------------	----

2.2 Material Used	27
2.2.1 ZnO.....	27
2.2.2 Silver (Ag).....	28
2.3 Deposition Techniques.....	28
2.3.1 Spin coating.....	29
2.3.2 Physical Vapor Deposition (PVD).....	30
2.4 Characterization Techniques.....	31
2.4.1 Field Emission Scanning Electron Microscope	31
2.4.2 X-ray diffraction.....	33
2.4.3 UV-Visible Spectroscopy	35
2.4.4 Photoluminescence Spectroscopy	37
2.4.5 Current-Voltage (I-V) Characterization	38
3. Silver Nanoparticle Decorated ZnO Nanorod Array Based Highly Sensitive Photodetector	43
3.1 Introduction	43
3.2 Experimental Details	45
3.3 Results and Discussions.....	47
3.3.1 Growth of ZnO nanorods:	47
3.3.2 Deposition of silver nanoparticle:	48
3.3.3 Optical Characterization:	49
3.3.4 Electrical characterization:.....	56
4. Conclusions and Future Scope.....	67
4.1 Conclusions:	67
4.2 Future scope.....	68

List of Figures

Figure 1.1: Photoconductor.....	2
Figure 1.2: Photodiode.....	2
Figure 1.3: Phototransistor.....	3
Figure 1.4: ZnO Wurtzite structure.....	6
Figure 1.5 Different morphologies of ZnO nanostructure ¹	8
Figure 1.6: Working mechanism of ZnO-based UV-photodetector.	13
Figure 1.7 Electric field and charge distribution at the surface of metal nanoparticles.	13
Figure 2.1: Spin coating technique	29
Figure 2.2: Physical Vapor Deposition Technique by thermal evaporation.....	30
Figure 2.3: Schematic of Field Emission Scanning Electron Microscope.....	32
Figure 2.4: Schematic diagram of Bragg's law.....	35
Figure 2.5: Schematic diagram of UV-visible spectrometer.	37
Figure 2.6: Schematic of PL measurement setup.....	38
Figure 3.1: Experimental Plan	46
Figure 3.2: Experimental procedure schematic	47
Figure 3.3: Schematic of Ag nanoparticles deposition	48
Figure 3.4: Ag nanoparticle deposition mechanism.....	49
Figure 3.5: FESEM image of a) S0 sample (pristine ZnO), the inset shows it's EDS spectra b) S5 sample (Ag-ZnO), the inset shows EDS spectra c) S20 sample (Ag-ZnO) d) S50 sample (Ag-ZnO).	50
Figure 3.6: a) FESEM image of S50 sample b) Elemental mapping of silver c) Edx spectra & elements weight % d) Elemental mapping of Zinc e) Elemental mapping of oxygen f) Edx silver weight % vs silver deposition time.....	51
Figure 3.7: XRD plots for all the samples	52
Figure 3.8: UV-Vis's absorption spectra of pristine ZnO and Ag-ZnO NRs	54
Figure 3.9: Tauc plot of pristine ZnO and Ag-ZnO NRs	55

Figure 3.10: Photoluminescence spectra of pristine ZnO and Ag-ZnO NRs	56
Figure 3.11: Device Structure Ag-ZnO.....	56
Figure 3.12: Photosensitivity & responsivity vs. silver deposition time.	57
Figure 3.13: Semi-log I-V characteristics of pristine ZnO and Ag-ZnO devices.....	58
Figure 3.14 Energy level diagram for a) S5 and S10 devices (smaller Ag -NPs based) b) S20 and S50 devices (Larger Ag-NPs based).....	59
Figure 3.15: Switching Response time graph of a) S0 (pristine ZnO) at 20V bias b) S5 (Ag-ZnO) at 20V bias c) S10 at 20V bias d) S5 at 0V bias devices.	60
Figure 3.16: Switching Response time graph of a) S5 b) S10 c) S0, with rise time and fall time calculation.	61
Figure 3.17: Current response vs No. of bending cycle.....	62
Figure 3.18: Schematic of the depletion region mechanism formation of a) for all the devices in the darkness. b) S5, S10 device under UV light illumination c) for S20, S50 device under UV light illumination	64

List of Tables

Table 1: Photosensitivity, responsivity, and Specific Detectivity of different devices.....	63
Table 2: Comparison of Sensitivity, R_{uv} / R_{vis} , and responsivity of reported devices and our device.....	65

List of Nomenclature & Acronyms

Nomenclature

α	Absorption coefficient
λ	Wavelength (nm)
d	Lattice spacing
e	Electronic charge
E_g	Bandgap energy
h	Planck's constant
I	Incident light intensity
I_d	Dark current
I_{ph}	Photocurrent
V_O	Oxygen Vacancy
Zn_i	Zinc Interstitial
P_O	Optical power intensity
E_f	Fermi level

Acronyms

A	Absorbance
DI	De-ionized
DLE	Defect Level Emission

EDX	Energy Dispersive X-ray
EQE	External Quantum Efficiency
HMTA	Hexamethylenetetramine
NBE	Near Band Emission
NPs	Nanoparticles
NRs	Nanorods
PL	Photoluminescence
PCR	Photochemical Reduction
PVD	Physical Vapor Deposition
R	Photoresponsivity
S	Photosensitivity
T	Transmittance
UV	Ultraviolet
XRD	X-Ray diffraction
ZnO	ZincOxide

Chapter 1

Introduction

1.1 Photodetector:

A photodetector is a device that senses and converts light into an electrical signal. A photodetector changes its conductivity whenever subjected to light illumination. Whenever light falls on the device and if the photon energy of the incoming light is greater than the bandgap energy of semiconductor material, electrons and hole pairs are photogenerated. These electron-hole pairs can be separated and can be collected at the metal electrodes with the help of applied bias to change conductivity in I-V characteristics. These days photodetector finds various applications in optical communication, missile tracking systems, inter-satellite communication, imaging Systems, environmental monitoring, medical diagnostics, astronomy, security and surveillance, Industrial automation, LIDAR systems, and consumer electronics. [1-4]

1.1.1 Types of photodetectors:

Based on the architecture of the device, the following are the types of photodetectors:

1. **Photoconductor:** Photoconductive detectors utilize semiconductors whose conductivity increases when exposed to light. Typically, the device consists of a photoconductive material (such as ZnO, CdS, or PbS) sandwiched between two ohmic contacts. In the absence of light, the device exhibits a high resistance. When exposed to light, photons with energy greater than the bandgap are absorbed, generating non-equilibrium

electron-hole pairs. These carriers reduce the material's resistance, allowing more current to flow under an applied bias voltage as shown in Figure 1.1 [5]

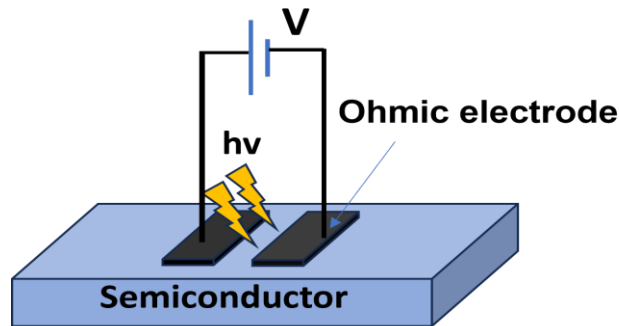


Figure 1.1: Photoconductor.

2. **Photodiode:** A photodiode is a p-n or PIN junction semiconductor device designed to operate under reverse bias. When photons strike the depletion region and have sufficient energy, they excite electrons from the valence to conduction band via the inner photoelectric effect, creating electron-hole pairs. The built-in electric field in the depletion region immediately separates these carriers: electrons drift to the cathode and holes to the anode, resulting in a measurable photocurrent as shown in Figure 1.2. The total output current is the sum of the photocurrent and a small dark current (leakage in absence of light), the latter of which should be minimized for higher sensitivity. [6]

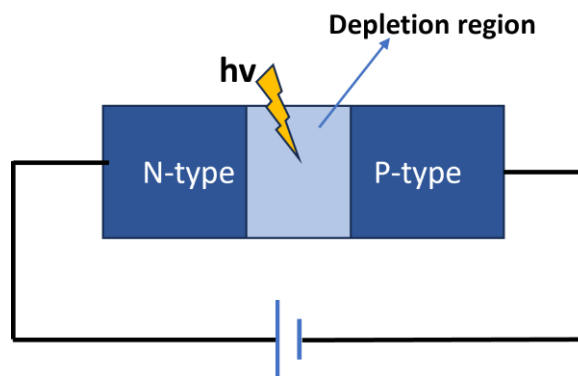


Figure 1.2: Photodiode.

3. Phototransistor: Phototransistors are essentially bipolar junction transistors (BJTs) with their base region exposed to light instead of being connected electrically. When photons generate carriers in the base region, it acts like a base current and triggers conventional transistor action. As a result, a small light-induced base current is amplified, leading to a much larger collector current as shown in Figure 1.3. This property makes phototransistors highly sensitive, especially in low-light environments, though at the cost of slower response time compared to photodiodes.

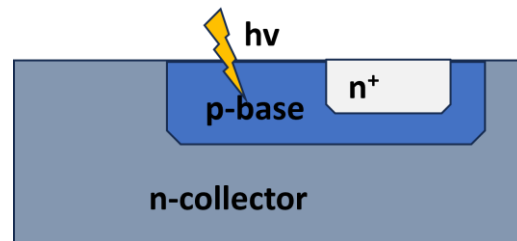


Figure 1.3: Phototransistor

Ultraviolet (UV) photodetectors (PDs): have become crucial tools in a wide range of applications due to their ability to detect and measure UV radiation. UV PDs play a significant role in both skin disease detection and environmental monitoring. In the field of dermatology, UV PDs are used in devices that monitor UV radiation exposure, which is a key factor in the development of skin conditions such as sunburn, premature aging, and skin cancer. These detectors are essential in UV dosimeters, which measure cumulative UV exposure, helping to prevent overexposure and reducing the risk of skin diseases. UV photodetectors have diverse applications beyond medical and environmental monitoring [7-8]. UV photodetectors are used in missile warning systems and flame detection, providing early alerts in critical situations. They are also increasingly integrated into consumer electronics, like UV index sensors in wearables and smartphones, for real-time monitoring of UV exposure. Most conventional UV photodetectors are based on thin film technology. While this approach has been effective, it often limits

the sensitivity and light absorption capabilities of the device. To overcome these limitations, researchers are exploring the use of one-dimensional (1D) and two-dimensional (2D) nanostructures. These nanostructured materials offer significantly larger surface areas compared to thin films, enhancing the interaction between the UV light and the sensing material. This increased surface area results in greater sensitivity and responsiveness, making 1D and 2D nanostructured photodetectors particularly well-suited for applications requiring precise UV detection. As research continues, the development of these advanced photodetectors is expected to provide more reliable, efficient, and sensitive tools for a broad range of applications. Additionally, the bandgap of materials can be adjusted by altering the size, shape, and morphology of nanostructures. Wide bandgap semiconductor materials such as GaN (3.4 eV), ZnO (3.37 eV), TiO₂ (3.2 eV), SnO₂ (3.6 eV), ZnTe (2.26 eV), ZnSe (2.7 eV), ZnS (3.7 eV), SiC (3.0 eV), Ga₂O₃ (4.9 eV), Nb₂O₅ (3.4 eV), WO₃ (2.6–2.8 eV), and NiO (3.7 eV). have been extensively studied for the development of UV photodetectors [9-18]. These wide bandgap metal oxide semiconductors offer excellent thermal and chemical stability, making them suitable for use in harsh environmental conditions. In this study, we utilized ZnO nanostructures to construct a UV photodetector.

1.2 ZnO

Zinc oxide (ZnO) is a versatile semiconductor material with a wide range of applications due to its unique physical, chemical, and electrical properties. It is a compound semiconductor with a wide direct bandgap of approximately 3.37 eV at room temperature, making it highly suitable for optoelectronic applications [19] such as ultraviolet (UV) light emitters, photodetectors, and transparent conductive oxides. ZnO also exhibits strong piezoelectric and pyroelectric properties, which are utilized in sensors, actuators, and energy-harvesting devices.

1.2.1 Structural Properties

Zinc oxide (ZnO) primarily crystallizes in the wurtzite structure, which is a hexagonal close-packed (hcp) lattice system and represents its most thermodynamically stable form under ambient conditions [20]. The unit cell of this structure is defined by lattice parameters $a \approx 3.25 \text{ \AA}$ and $c \approx 5.207 \text{ \AA}$, giving a c/a ratio of ~ 1.58 , which is close to the ideal value for hexagonal symmetry [21]. In this configuration, each Zn^{2+} ion is tetrahedrally coordinated to four O^{2-} ions, and vice versa, forming a highly stable three-dimensional framework. This tetrahedral coordination is a key feature that governs many of ZnO's remarkable properties, such as its wide bandgap ($\sim 3.37 \text{ eV}$), high exciton binding energy, and piezoelectric behavior. One of the most distinctive characteristics of the wurtzite structure is its polar nature. Along the crystallographic c -axis ($[0001]$ direction), the lattice consists of alternating planes of positively charged zinc and negatively charged oxygen atoms. This results in two oppositely charged polar surfaces: the Zn-terminated (0001) surface and the O-terminated $(000\bar{1})$ surface. These polar facets lead to intrinsic dipole moments, which significantly influence the growth kinetics of ZnO nanostructures, promote anisotropic elongation along the c -axis, and affect surface reactivity and chemical sensing performance as illustrated in Figure 1.4, this unique crystal polarity, combined with strong ionic bonding and tetrahedral geometry, makes ZnO an excellent candidate for applications in piezoelectric sensors, optoelectronic devices, and UV photodetectors. The ability of ZnO to form one-dimensional nanostructures such as nanorods and nanowires is directly linked to this wurtzite structural anisotropy and surface energy distribution.

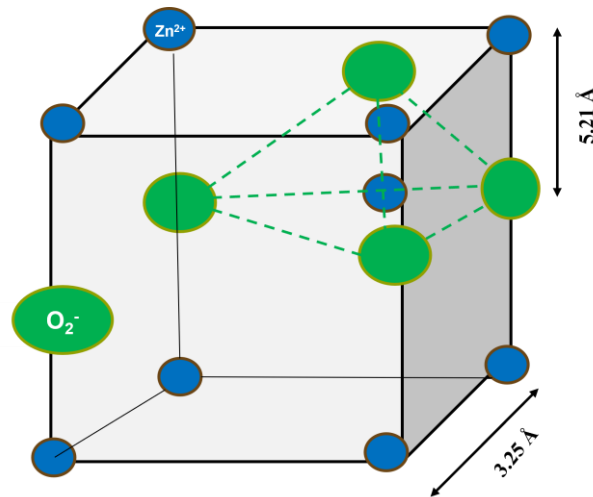


Figure 1.4: ZnO Wurtzite structure

1.2.2 Optoelectronic properties

The ZnO has a wide bandgap of 3.37 eV which makes it a suitable choice for UV photodetector applications. It has a high exciton binding energy of 60 meV. Due to this, the excitons in ZnO are more stable and can exist at higher temperatures without dissociating into free electrons and holes [22]. ZnO also has high electron mobility which increases the response speed. ZnO is highly transparent in the visible range of the spectrum, making it an excellent material for transparent electronics. Furthermore, ZnO can be doped & coated with various elements to tailor its electrical and optical properties. For instance, doping with group III elements (such as aluminum or gallium) can increase conductivity, making ZnO a better transparent conductive oxide, and also coating with metal NPs (such as gold and silver) can enhance its various performance parameters such as sensitivity, responsivity, response speed, etc.

1.2.3 ZnO Nanostructures

Zinc oxide (ZnO) nanostructures have garnered significant interest due to their remarkable properties, which are distinct from those

of their bulk counterparts, enabling their use in diverse applications across electronics, optoelectronics, sensing, energy harvesting, and biomedical fields. These nanostructures can exist in various forms as shown in Figure 1.5 [23], each with unique physical, chemical, and optical characteristics. For instance, ZnO nanowires and nanorods are one-dimensional (1D) structures with high aspect ratios, known for their excellent charge transport properties and high surface-to-volume ratio, making them ideal for use in photodetectors, sensors, and energy-harvesting devices. Two-dimensional (2D) ZnO structures, such as nanosheets and nanoplates, possess large surface areas, making them suitable for applications in gas sensing, catalysis, and as transparent conductive films. Meanwhile, zero-dimensional (0D) structures like nanoparticles and quantum dots, typically smaller than 10 nm, benefit from quantum confinement effects, resulting in tunable electronic and optical properties. These structures are utilized in biomedical imaging, drug delivery, and UV-blocking coatings. Moreover, more complex three-dimensional (3D) structures, such as nanoflowers and nano-tetrapods, offer enhanced surface interactions, making them advantageous for photocatalysis and advanced sensing applications.

1.2.4 Synthesis of ZnO nanostructure:

The morphology, defect states, and crystallinity of ZnO nanostructures play a crucial role in determining their optoelectronic and sensing properties. Consequently, significant efforts have been dedicated to synthesizing a diverse array of highly crystalline ZnO nanostructures, including morphologies such as nanorods, nanoplates, nanowires, nanoflowers, and nano-tetrapods. The synthesis techniques for ZnO nanostructures can be broadly categorized into two main groups: gas-phase and liquid-phase synthesis.

Gas-phase synthesis techniques encompass methods such as chemical vapor deposition (CVD), metal-organic chemical vapor deposition (MOCVD), physical vapor deposition (PVD), pulsed laser deposition (PLD), molecular beam epitaxy (MBE), electron beam

deposition, and organometallic vapor epitaxy (OMVPE) [24-29]. Among these, physical vapor deposition methods, like thermal evaporation, are commonly employed to deposit various ZnO nanostructures. In these systems, target materials are heated to their evaporation temperature, leading to the formation of thin films or nanostructures on the substrate. However, there is a considerable risk of catalyst and impurity incorporation into the ZnO lattice.

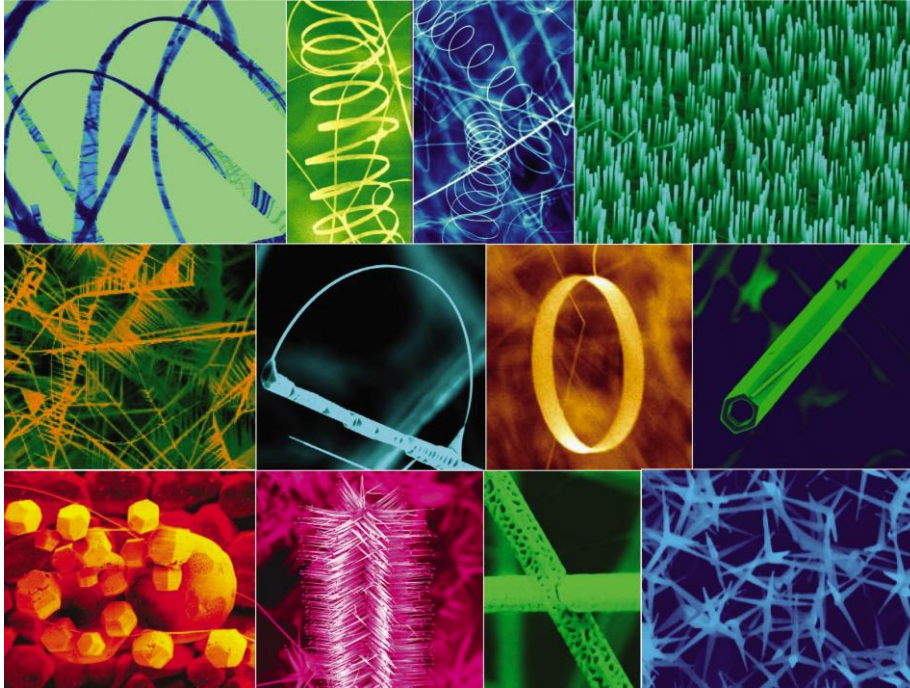


Figure 1.5 Different morphologies of ZnO nanostructure¹

CVD is another well-established technique that offers excellent control over crystallinity, uniformity, and defect density. A basic CVD setup typically consists of a vacuum chamber, precursor gases, and substrate heaters. Chemical reactions occur near or on the heated substrate, within a temperature range of 200 °C to 1600 °C, resulting in the growth of uniform and high-quality thin films. One significant advantage of the CVD process is its ability to provide a uniform coating on substrates with varied geometries. Moreover, deposition can occur at lower vacuum pressures compared to PVD systems. This method can produce a variety of ZnO nanostructures, such as nanowires, nanoropes,

¹Reprinted from Materials Today, Volume 7, Issue 6, Zhong Lin Wang, Nanostructures of zinc oxide, 26-33, Copyright (2004), with permission from Elsevier.

nanorods, nanotips, and nanowalls, However, CVD has limitations, including low production yield and a restricted choice of substrates

Gas-phase deposition techniques such as chemical vapor deposition (CVD), thermal evaporation, and molecular beam epitaxy (MBE) are capable of producing highly crystalline thin films and nanostructures. However, they typically require ultra-high vacuum ($\sim 10^{-6}$ mbar) and high processing temperatures (200–1600 °C), making them costly and less suitable for flexible organic substrates.

In comparison, liquid-phase synthesis methods—including spray pyrolysis, sol-gel processing, hydrothermal growth, and electrospinning—operate at lower temperatures (typically 80–200 °C) and ambient pressures. These methods are more compatible with flexible substrates and are better suited for large-scale, economical production. Among them, hydrothermal synthesis is particularly advantageous due to its ability to produce diverse ZnO nanostructures by simply adjusting precursor composition and reaction conditions, as shown in Figure 1.5.

Therefore, in this study, the hydrothermal method was selected for its low processing temperature, compatibility with flexible substrates, and scalability—making it ideal for cost-effective fabrication of ZnO-based devices.

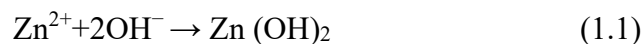
Here in this research work, we have utilized the hydrothermal technique to fabricate ZnO nanorods (NRs), the necessary steps involved in the fabrication of the photodetector are listed below:

1. Initially, a seed layer of ZnO is deposited on the concave side of the polyimide substrate using a spin-coating technique. This is done with a solution of 3M zinc acetate and ethanolamine dissolved in 2-methoxyethanol. The ZnO nanoparticles within the seed layer serve as nucleation sites for the subsequent growth of nanorods.

2. After thin film deposition, the samples are annealed at 240°C to improve the adhesion between the thin film and the polyimide substrate.
3. A growth solution is then prepared using hexamethylenetetramine (HMTA) as the basic compound and zinc nitrate ($\text{Zn}(\text{NO}_3)_2$). HMTA supplies OH^- ions, while zinc nitrate provides Zn^{2+} ions, leading to the formation of $\text{Zn}(\text{OH})_2$, which is thermodynamically unstable and decomposes into ZnO , resulting in the growth of ZnO nanorods.
4. Finally, the hydrothermal growth process is performed by immersing the thin-film samples in the prepared growth solution at **110 °C** for a duration of **3 hours**. Upon completion of the growth, the samples are carefully removed from the solution, thoroughly rinsed with deionized water to eliminate any residual precipitates, and then air-dried under ambient conditions to remove excess moisture.

The following is the proposed growth mechanism for the growth of ZnO nanorods: Commonly, zinc nitrate and hexamethylenetetramine (HMTA) are used as precursors in the growth solution. During the growth process, the following chemical reactions occur [31]:

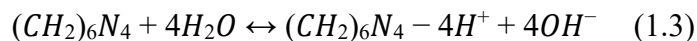
Formation of $\text{Zn}(\text{OH})_2$:

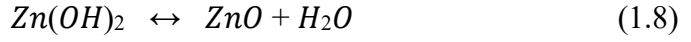
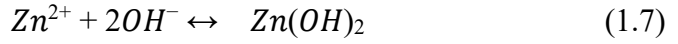
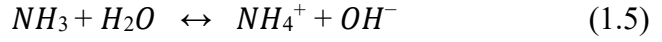


Decomposition to ZnO :



These reactions lead to the continuous supply of Zn^{2+} and OH^- ions, facilitating the sustained growth of ZnO nanorods along the c-axis direction. By adjusting the concentration of the precursors and additives, various morphologies of ZnO nanostructures can be achieved.





In contrast to the growth in an alkaline solution where OH^- ions are directly supplied by the solution, in the current system, water molecules in the solution provide the OH^- ions. Hexamethylenetetramine (HMTA) acts as a pH buffer, ensuring a consistent supply of OH^- ions in the precursor solution through its decomposition (as described in Eq. 1.3). The hydrolysis of HMTA results in the production of ammonia (NH_3) and formaldehyde ($HCHO$). The rate of HMTA decomposition is influenced by the pH and temperature of the solution. Ammonia serves two crucial functions: first, it maintains a constant supply of OH^- ions, and second, it forms a complex with Zn^{2+} ions, thereby regulating their availability in the solution.

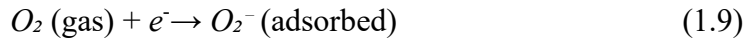
The Zn^{2+} ions subsequently react with the OH^- ions to form $Zn(OH)_2$, which is thermodynamically unstable and decomposes into ZnO [32]. HMTA not only promotes the growth of ZnO along the c-axis but also adheres to the nonpolar side facets of the nanostructures, inhibiting lateral growth. This selective inhibition allows ZnO molecules to preferentially deposit on the (0001) plane, resulting in the formation of high aspect ratio ZnO nanorods [33-34].

1.2.5 Working of ZnO nanostructured-based UV PDs

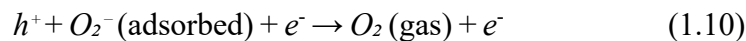
ZnO -based one-dimensional (1D) and two-dimensional (2D) nanostructures have a high surface-to-volume ratio, making them highly sensitive to optical, physical, and chemical changes in their surroundings. As a result, ZnO is extensively utilized in the development of highly sensitive and responsive nanoscale light sensors. The fundamental principle of photodetection involves the internal

photoelectric effect: when light strikes the surface of a semiconductor, and if the energy of the incident photons ($E_{ph} = hc/\lambda$) is greater than the material's energy bandgap (E_g), the incident light is absorbed. As a result, electron-hole pairs are generated within the semiconductor material. These pairs can be separated by applying an external electric field, causing the charge carriers to move toward their respective electrodes, ultimately generating a photocurrent. The magnitude of this photocurrent is directly related to the intensity of the light incident on the device.

Figure 1.6 illustrates the photodetection mechanism in nanorods. In photodetectors based on ZnO nanorods, oxygen adsorption and desorption processes are essential for their functionality. In the dark conditions, oxygen molecules from the atmosphere gets chemically adsorbed onto the surface of ZnO nanorods (NRs), by capturing thermally excited electrons from the conduction band (CB) of ZnO, hence thereby forming a depletion region (low conductive region) inside ZnO CB leading to lower dark current [35]. The reaction process is given as,



When UV light is illuminated, photogenerated electron-hole pairs are formed inside ZnO NRs, and further, some of the holes react with oxygen molecules, causing the desorption of oxygen molecules from the ZnO NRs surface, by releasing the captured electrons from oxygen molecule, hence reducing the depletion region width inside ZnO NRs, thereby enhancing photocurrent inside ZnO CB. The reaction process is given as,



The available photogenerated free electrons, along with available holes, contribute to an increase in photocurrent through ZnO NSs under the influence of the externally applied bias. Numerous studies highlight the influence of ambient conditions on photoresponse behavior. It has been observed that the photoresponse is slower under

vacuum conditions and significantly faster in the presence of air, underscoring the crucial role of oxygen in this process [35-36].

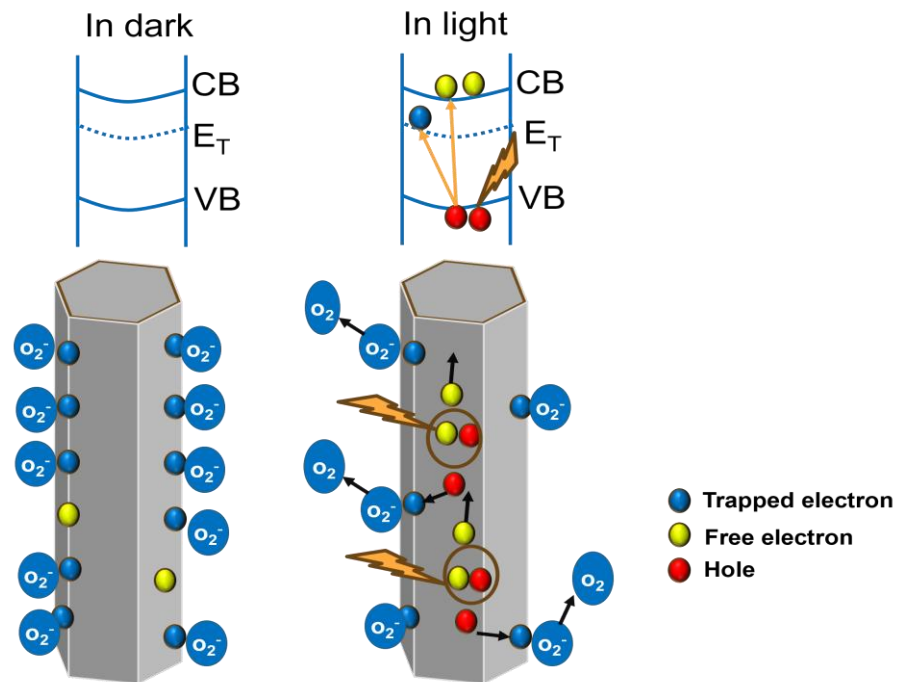


Figure 1.6: Working mechanism of ZnO-based UV-photodetector.

1.3 LSPR (Localized Surface Plasmon Resonance)

Localized Surface plasmon resonance (LSPR) occurs when light interacts with metal nanoparticles, causing collective oscillations of the

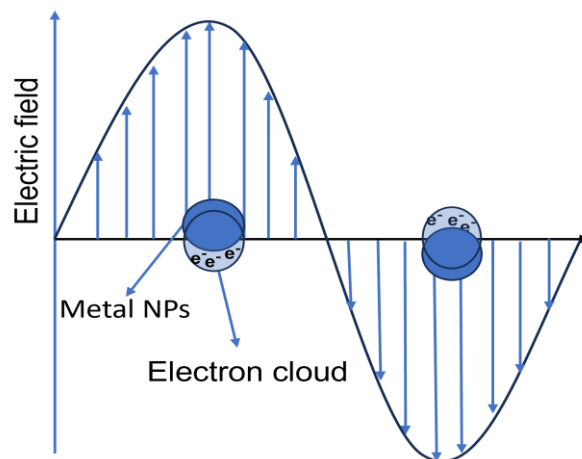


Figure 1.7 Electric field and charge distribution at the surface of metal nanoparticles.

conduction electrons as shown in Figure 1.7, especially in metals like silver, gold, aluminum, etc. In their nanoparticle form, these metals can absorb light in the UV or visible region by transferring the energy of light to the oscillating electrons leading to the formation of highly energetic hot electrons inside metal NPs, especially for the smaller-sized metal nanoparticles (0 to 30nm) [37]. Upon UV-Visible light excitation, localized surface plasmon resonance (LSPR) in Ag nanoparticles results in the generation of hot electrons. The hot electrons generated in silver nanoparticles raise the Fermi level locally. These energetic electrons can tunnel or transfer into the conduction band of ZnO. This transfer improves electron density in ZnO and facilitates effective charge separation, thereby significantly enhancing device metrics such as photosensitivity and responsivity.

Silver NPs show an absorption peak in the UV-Vis absorption spectra near 410 nm due to the plasmonic frequency. The plasmonic frequency, also known as the surface plasmon resonance (SPR) frequency, is a fundamental characteristic of metallic nanoparticles such as silver (Ag) nanoparticles (NPs). This frequency corresponds to the oscillation of conduction electrons on the nanoparticle's surface in resonance with the electromagnetic field of incident light, leading to a notable absorption or scattering peak.

The plasmonic resonance is influenced by various factors including the nanoparticle's size, shape, and the dielectric properties of its surrounding environment. For bulk metals, the plasmonic frequency ω_p is mathematically expressed as:

$$\omega_P = \sqrt{\frac{ne^2}{\epsilon_0 m^*}} \quad (1.11)$$

where n (electron density) is the number of conduction electrons per unit volume, e is the elementary charge, m^* is the effective mass of the conduction electron, ϵ_0 is the permittivity of free space. Equation (1.11), the plasma frequency is given by: $\omega_p = \sqrt{(ne^2 / \epsilon_0 m)^*}$ where n is the free electron density (approximately $5.8 \times 10^{22} \text{ cm}^{-3}$ for silver), e is the

elementary charge, m^* is the effective mass of the electron (approximately 9.1×10^{-31} kg), and ϵ_0 is the vacuum permittivity. For silver (Ag), this plasma frequency corresponds to a surface plasmon resonance (SPR) in the visible region, typically around 410 nm with a value of 4.60×10^{15} rad/s.

Oscillating electrons in metal nanoparticles can decay via two primary pathways: radiative and non-radiative. In non-radiative decay, the energy of these electrons is transferred to nearby atoms, resulting in localized heating and an increase in the temperature of the surrounding environment. For small nanoparticles absorption dominates due to enhanced light-matter interaction, leading to the generation of highly energetic hot electrons. These hot electrons elevate the local Fermi level of the nanoparticle. When a semiconductor such as ZnO is in contact with the metal nanoparticle, the hot electrons can be transferred into the semiconductor to achieve Fermi level alignment, thereby enhancing the device's photoresponse. In the absence of an adjacent semiconductor or when nanoparticles are isolated, the hot electrons generated within the metal nanoparticle undergo rapid energy loss through phonon-mediated relaxation, resulting in heat dissipation within the nanoparticle itself [38].

As the size of the silver nanoparticles increases, scattering becomes the dominant mechanism. Larger nanoparticles favor radiative decay, wherein the energy of oscillating electrons is released as scattered light rather than being absorbed and converted into hot electrons. Consequently, the efficiency of hot electron transfer to adjacent semiconductors diminishes in larger nanoparticles, as more energy is lost radiatively rather than being harnessed for charge injection [38].

The size of Ag nanoparticles plays a critical role in determining their interaction with light. For diameters <30 nm, absorption dominates due to localized surface plasmon resonance (LSPR), facilitating hot electron generation. Conversely, for diameters >100 nm, scattering becomes dominant, often leading to reduced carrier injection efficiency. In this study, optimal photodetector performance was achieved when

silver nanoparticles (Ag NPs) of size ranging from 5–30 nm were synthesized through short-duration UV irradiation (254 nm) for 5–10 seconds. This exceptional enhancement is attributed primarily to the dominance of the hot electron injection mechanism over plasmonic scattering losses. The smaller Ag NP sizes formed under shorter UV exposure times are particularly advantageous, as they not only ensure better interface coupling with the ZnO nanorods but also facilitate more efficient charge transfer. Consequently, these conditions result in superior photocarrier generation and separation, thereby boosting responsivity. These findings establish a clear correlation between UV exposure time, Ag NP size, and the resulting photo-sensing characteristics, highlighting the critical role of precisely tuned surface plasmon effects in enhancing UV photodetector performance [39].

1.3.1 Applications of Nanoplasmonics:

The high absorption coefficient linked to the excitation of localized surface plasmons (LSPs) unlocks a wide array of potential applications for metallic nanoparticles across various fields. LSPs offer the ability to concentrate, amplify, and manipulate light at the nanoscale, enabling the enhancement of optical effects or the activation of specific processes with precision. Numerous studies have extensively documented the diverse applications of LSPs in various areas. To illustrate the versatility of LSPs, we will focus on three key areas: biomedicine, energy, and the environment. However, the primary focus here is on energy applications, as the main goal of this thesis is the development of plasmonic-based optoelectronic devices.

1.4 Challenges:

ZnO, as a wide bandgap material, holds great potential for near-UV detection applications. However, pure ZnO faces challenges such as low photosensitivity, limited photoselectivity, and reduced carrier mobility due to intrinsic defects and high radiative recombination

associated with its large exciton binding energy. This requires a substantial voltage bias to effectively separate the photogenerated electron-hole pairs, leading to low efficiency in UV photodetectors where efficient charge separation is vital. To address these issues and to improve key performance metrics like sensitivity, selectivity, and response speed, metal nanoparticles like silver are commonly integrated onto the surface of ZnO nanostructures (NSs) [40].

Furthermore, ZnO nanostructures synthesized via hydrothermal methods often exhibit poor adhesion to substrates, compromising the flexibility of the devices. These nanostructures are also susceptible to various intrinsic defects, which can significantly impact device performance by reducing carrier mobility. Therefore, enhancing the adhesion of thin films by annealing of the seed layer at high temperature, and reducing defect concentrations in hydrothermally grown ZnO nanostructures by the addition of additives such as KMnO_4 are essential steps to improve the sensitivity and responsiveness of these devices [41].

Ambient conditions also significantly impact device stability, response time, and sensitivity. As mentioned earlier, the adsorption and desorption of oxygen under dark and light-exposed conditions, respectively, play a crucial role in device performance. These processes tend to be slow, which can limit the device's response speed. The incorporation of metal nanoparticles such as silver could enhance response speed due to the formation of the Schottky junction at the Ag-ZnO interface.

With the growing demand for flexible and wearable UV sensors, such as wearable UV dosimeters, various flexible substrates like polyimide, paper, and PET, have been explored. However, significant progress is still required in this area. Consequently, it is crucial to develop ZnO nanostructures on flexible substrates, that can deliver strong UV sensing performance metrics like sensitivity, selectivity, and response speed.

1.5 Review of past work:

ZnO is a wide bandgap material, which is highly interesting for UV photodetector applications, due to its high mobility, cost-effectiveness, biocompatibility, non-toxicity, high exciton binding energy, etc. In the past researchers have demonstrated plasmonic coupling between metal nanoparticles and ZnO nanostructures and its effect on the optoelectronic properties of ZnO [40]. Many research articles have been published to enhance the photosensitivity, photo-selectivity, response speed, and stability of the UV photodetector. Yen et al. have improved the photosensitivity of the device by depositing silver nanoparticles on the ZnO nanostructure grown by RF Magnetron sputtering [41]. In another work, Anil et al. have also improved response speed by incorporating silver nanoparticles on the hydrothermally grown ZnO honeycomb structure [42]. Jitesh et al. successfully fabricated a highly visible-blind UV photodetector by precisely controlling defects during the hydrothermal growth process to produce customized ZnO nanostructures [43]. Further, Yi Chen et al. have enhanced the UV absorption by incorporating silver nanoparticles on the ZnO Nanorod array on mechanical flexible substrates [44]. While numerous studies focus on developing ZnO nanostructured photodetectors with high responsivity and rapid response speed, there are only a limited number of reports addressing enhanced stability, sensitivity, and response time in fully solution-processed Ag-decorated ZnO nanostructure-based UV photodetectors.

1.5.1 Objectives of this work

1. To develop a highly-photosensitive UV photodetector for flexible and wearable electronics.
2. To optimize the deposition of silver nanoparticles (Ag-NPs) using the solution-processed photochemical reduction (PCR) method.
3. To optimize the size of silver NPs deposited on ZnO NRs, for effectively optimizing the plasmonic coupling effect between Ag-NPs and ZnO Nanorods.

4. To enhance performance parameters such as photosensitivity, photoselectivity, responsivity & stability of the fabricated device.
5. To improve the adhesivity of the hydrothermally grown ZnO nanostructures with polyimide substrate, to enhance the flexibility of the device.

1.6 Organization of Thesis

- In **Chapter 1**, we have started our discussion on different types of photodetectors based on device configuration and discussed their working principle. Then, we briefly discussed UV photodetectors and wide bandgap materials. Further, we also discussed the ZnO nanostructure-based MSM UV photodetector in detail.
- In **Chapter 2**, we have discussed the experimental procedure for the growth of Ag-ZnO nanostructures and various deposition techniques. Further, the different optical and electrical characterization techniques have been discussed in detail.
- In **Chapter 3**, a high-sensitivity UV photodetector is developed using Ag-deposited ZnO nanorods.
- **Chapter 4** presents the conclusion of the work done and the future scope of the presented work.

References

Chapter 1

- [1] A. B. Djurišić, A. M. C. Ng, and X. Y. Chen, "ZnO nanostructures for optoelectronics: Material properties and device applications," *Prog. Quantum Electron.*, vol. 34, no. 4, pp. 191–259, 2010, doi: 10.1016/j.pquantelec.2010.04.001.
- [2] Y. Vaynzof, D. Kabra, T. J. K. Brenner, H. Sirringhaus, and R. H. Friend, "Recent Advances in Hybrid Optoelectronics," *Int. J. Chem.*, vol. 496, pp. 517–524, 2012, doi: 10.1002/ijch.201100108.
- [3] C. Klingshirn, "ZnO: From basics towards applications," *Phys. Status Solidi B*, vol. 244, no. 9, pp. 3027–3072, 2007, doi: 10.1002/pssb.200743072.
- [4] F. Omnès, E. Monroy, E. Muñoz, and J. L. Reverchon, "Wide bandgap UV photodetectors: A short review of devices and applications," in *Gallium Nitride Materials and Devices II*, vol. 6473, p. 64730E, 2007, doi: 10.1117/12.705393.
- [5] J. Agrawal, T. Dixit, I. A. Palani, and V. Singh, "Development of Al-Doped ZnO Nanowalls Based Flexible, Ultralow Voltage UV Photodetector," *IEEE Sensors Lett.*, vol. 3, no. 9, Art. no. 3501504, Sep. 2019, doi: 10.1109/LENS.2019.2938638.
- [6] J. H. He, S. Te Ho, T. B. Wu, L. J. Chen, and Z. L. Wang, "Electrical and photoelectrical performances of nano-photodiode based on ZnO nanowires," *Chem. Phys. Lett.*, vol. 435, no. 1-3, pp. 119–122, 2007, doi: 10.1016/j.cplett.2006.12.061.
- [7] Y.-L. Chu et al., "Fabrication and characterization of UV photodetectors with Cu-doped ZnO nanorod arrays," *J. Electrochem. Soc.*, vol. 167, no. 2, Art. no. 027522, Jan. 2020, doi: 10.1149/19457111/ab69f2.
- [8] C.-H. Huang et al., "Fabrication and characterization of homostructured photodiodes with Li-doped ZnO nanorods," *Microsyst. Technol.*, vol. 28, no. 1, pp. 369–375, Apr. 2020, doi: 10.1007/s00542-020-04854-1.
- [9] M. Shaygan et al., "Highly sensitive photodetectors using ZnTe/ZnO core/shell nanowire field effect transistors with a tunable core/shell ratio," *J. Mater. Chem. C*, vol. 4, no. 10, pp. 2040–2046, 2016, doi: 10.1039/C5TC03999A.

- [10] E. Oksenberg, R. Popovitz-Biro, K. Rechav, and E. Joselevich, "Guided Growth of Horizontal ZnSe Nanowires and their Integration into High-Performance Blue–UV Photodetectors," *Adv. Mater.*, vol. 27, no. 27, pp. 3999–4005, 2015, doi: 10.1002/adma.201500736.
- [11] X. Fang et al., "Single-crystalline ZnS nanobelts as ultraviolet-light sensors," *Adv. Mater.*, vol. 21, no. 20, pp. 2034–2039, 2009, doi: 10.1002/adma.200802441.
- [12] A. Aldalbahi et al., "A new approach for fabrications of SiC-based photodetectors," *Sci. Rep.*, vol. 6, no. 1, Art. no. 23457, 2016, doi: 10.1038/srep23457.
- [13] E. Monroy et al., "High-performance GaN pn junction photodetectors for solar ultraviolet applications," *Semicond. Sci. Technol.*, vol. 13, no. 9, pp. 1042–1046, 1998, doi: 10.1088/0268-1242/13/9/013.
- [14] J. Agrawal, T. Dixit, I. A. Palani, and V. Singh, "Electron depleted ZnO nanowalls-based broadband photodetector," *IEEE Photon. Technol. Lett.*, vol. 31, no. 20, pp. 1639–1642, Oct. 2019, doi: 10.1109/LPT.2019.2940881.
- [15] G. Wang et al., "Hydrogen-treated TiO₂ nanowire arrays for photoelectrochemical water splitting," *Nano Lett.*, vol. 11, no. 7, pp. 3026–3033, 2011, doi: 10.1021/nl201766h.
- [16] M. Tarini, N. Prakash, I. M. M. Sahib, and Y. Hayakawa, "Novel sugar apple-shaped SnO₂ microspheres with light scattering effect in dye-sensitized solar cell application," *IEEE J. Photovoltaics*, vol. 7, no. 4, pp. 1050–1057, Jul. 2017, doi: 10.1109/JPHOTOV.2017.2698500.
- [17] Z. Hai et al., "Photodetector with superior functional capabilities based on monolayer WO₃ developed by atomic layer deposition," *Sens. Actuators B Chem.*, vol. 245, pp. 954–962, 2017, doi: 10.1016/j.snb.2017.02.009.
- [18] X. Chang et al., "UV-photodetector based on NiO/diamond film," *Appl. Phys. Lett.*, vol. 112, no. 3, Art. no. 032103, 2018, doi: 10.1063/1.5004269.
- [19] U. Pal et al., "Synthesis and optical properties of ZnO nanostructures with different morphologies," *Opt. Mater.*, vol. 29, no. 1, pp. 65–69, 2006, doi: 10.1016/j.optmat.2006.03.015.
- [20] F. R. Blom et al., "Thin-film ZnO as micromechanical actuator at low frequencies," *Sens. Actuators A Phys.*, vol. 21, no. 1-3, pp. 226–228, 1990, doi: 10.1016/0924-4247(90)85044-5.
- [21] Z. L. Wang, "Zinc oxide nanostructures: Growth, properties and applications," *J. Phys. Condens. Matter*, vol. 16, no. 25, pp. R829–R858, 2004, doi: 10.1088/0953-8984/16/25/R01.

- [22] D. K. Hwang et al., "p-ZnO/n-GaN heterostructure ZnO light-emitting diodes," *Appl. Phys. Lett.*, vol. 86, no. 22, Art. no. 222101, 2005, doi: 10.1063/1.1940736.
- [23] Z. Wang, "Nanostructures of Zinc Oxide," *Mater. Today*, vol. 7, no. 6, pp. 26–33, 2009, doi: 10.1016/S1369-7021(04)00286-X.
- [24] X. Xia et al., "High-quality metal oxide core/shell nanowire arrays on conductive substrates for electrochemical energy storage," *ACS Nano*, vol. 6, no. 6, pp. 5531–5538, 2012, doi: 10.1021/nn301454q.
- [25] W. Tian et al., "Flexible SnO₂ hollow nanosphere film-based high-performance ultraviolet photodetector," *Chem. Commun.*, vol. 49, no. 36, pp. 3739–3745, 2013, doi: 10.1039/C3CC39273B.
- [26] G. M. Ali and P. Chakrabarti, "Performance of ZnO-based ultraviolet photodetectors under varying thermal treatment," *IEEE Photon. J.*, vol. 2, no. 5, pp. 784–788, 2010, doi: 10.1109/JPHOT.201
- [27] G. M. Ali and P. Chakrabarti, "Performance of ZnO-based ultraviolet photodetectors under varying thermal treatment," *IEEE Photonics Journal*, vol. 2, no. 5, pp. 784–792, Oct. 2010, doi: 10.1109/JPHOT.2010.2054070.
- [28] A. Kumar, K. Bhargava, T. Dixit, I. A. Palani, and V. Singh, "Hydrothermal Processed ZnO Nanorod Networks Based Field Effect Transistors," *Journal of Electronic Materials*, vol. 45, no. 11, pp. 4768–4773, 2016, doi: 10.1007/s11664-016-4768-y.
- [29] W. J. E. Beek, M. M. Wienk, M. Kemerink, X. Yang, and R. A. J. Janssen, "Hybrid zinc oxide conjugated polymer bulk heterojunction solar cells," *The Journal of Physical Chemistry B*, vol. 109, no. 19, pp. 9505–9516, 2005, doi: 10.1021/jp050745x.
- [30] I. Udom, M. K. Ram, E. K. Stefanakos, A. F. Hepp, and D. Y. Goswami, "One-dimensional ZnO nanostructures: Synthesis, properties, and environmental applications," *Materials Science in Semiconductor Processing*, vol. 16, no. 6, pp. 2070–2083, 2013, doi: 10.1016/j.mssp.2013.06.017.
- [31] S. Xu and Z. L. Wang, "One-dimensional ZnO nanostructures: Solution growth and functional properties," *Nano Research*, vol. 4, no. 11, pp. 1013–1098, Nov. 2011, doi: 10.1007/s12274-011-0160-7.
- [32] Y. Sheng, Y. Jiang, X. Lan, C. Wang, S. Li, X. Liu, and H. Zhong, "Mechanism and Growth of Flexible ZnO Nanostructure Arrays in a Facile Controlled Way," *Journal of Nanomaterials*, vol. 2011, pp. 1–12, 2011, doi: 10.1155/2011/473629.

- [33] H. Wang, C. Xie, D. Zeng, and Z. Yang, "Controlled organization of ZnO building blocks into complex nanostructures," *Journal of Colloid and Interface Science*, vol. 297, no. 2, pp. 570–577, Dec. 2005, doi: 10.1016/j.jcis.2005.10.059.
- [34] D. Vernardou, G. Kenanakis, S. Couris, A. C. Manikas, G. A. Voyiatzis, M. E. Pemble, E. Koudoumas, and N. Katsarakis, "The effect of growth time on the morphology of ZnO structures deposited on Si (100) by the aqueous chemical growth technique," *Journal of Crystal Growth*, vol. 308, no. 1, pp. 105–109, Jan. 2008, doi: 10.1016/j.jcrysgro.2007.07.032.
- [35] C. Soci, A. Zhang, B. Xiang, S. A. Dayeh, D. P. Aplin, J. Park, X. Y. Bao, Y. H. Lo, and D. Wang, "ZnO nanowire UV photodetectors with high internal gain," *Nano Letters*, vol. 7, no. 4, pp. 1003–1009, Apr. 2007, doi: 10.1021/nl070111x.
- [36] Y. K. Su, S. M. Peng, L. W. Ji, C. Z. Wu, W. B. Cheng, and C. H. Liu, "Ultraviolet ZnO nanorod photosensors," *Langmuir*, vol. 26, no. 1, pp. 603–606, Jan. 2010, doi: 10.1021/la902171j.
- [37] H. H. Mai, et al., "Nonlinear optical properties of Ag nanoclusters and nanoparticles dispersed in a glass host," *The Journal of Physical Chemistry C*, vol. 118, no. 29, pp. 15995–16002, 2014, doi: 10.1021/jp502294u.
- [38] P. K. Jain, X. Huang, I. H. El-Sayed, and M. A. El-Sayed, "Noble Metals on the Nanoscale: Optical and Photothermal Properties and Some Applications in Imaging, Sensing, Biology, and Medicine," *Accounts of Chemical Research*, vol. 41, no. 12, pp. 1578–1586, Dec. 2008, doi: 10.1021/ar7002804.
- [39] P. K. Jain, K. S. Lee, I. H. El-Sayed, and M. A. El-Sayed, "Calculated absorption and scattering properties of gold nanoparticles of different size, shape, and composition: Applications in biological imaging and biomedicine," *The Journal of Physical Chemistry B*, vol. 110, no. 14, pp. 7238–7248, Apr. 2006, doi: 10.1021/jp057170o.
- [40] Y. L. Chu, S. J. Young, Y. J. Chu, Y. H. Liu, and T. T. Chu, "High-Performance UV Photodetectors Based on 1-D Ag/ZnO Nanostructures With a Simple Photochemical Process at Room Temperature," *IEEE Electron Device Letters*, vol. 44, no. 1, pp. 124–127, Jan. 2023, doi: 10.1109/LED.2022.3220753.
- [41] J. Agrawal, *Investigations on Hydrothermally Grown ZnO Nanostructures Towards Development of UV/Broadband Photodetectors*, Ph.D. thesis, Discipline of Electrical Engineering, Indian Institute of Technology Indore, India, Jan. 2020.
- [42] A. Yadav, J. Agrawal, and V. Singh, "Development of visible-blind UV photodetector using solution-processed Ag-ZnO nanostructures," *IEEE Photonics*

Technology Letters, vol. 33, no. 19, pp. 1065–1068, Oct. 2021, doi: 10.1109/LPT.2021.3103097.

[43] J. Agrawal, T. Dixit, I. A. Palani, and V. Singh, "Highly Visible-Blind ZnO Photodetector by Customizing Nanostructures With Controlled Defects," *IEEE Photonics Technology Letters*, vol. 32, no. 22, pp. 1439–1442, Nov. 2020, doi: 10.1109/LPT.2020.3031732.

[44] Y. Chen, W. H. Tse, L. Chen, et al., "Ag nanoparticles-decorated ZnO nanorod array on a mechanical flexible substrate with enhanced optical and antimicrobial properties," *Nanoscale Research Letters*, vol. 10, no. 106, pp. 1–10, Jan. 2015, doi: 10.1186/s11671-014-0712-3.

Chapter 2

[45] U. Pal, J. G. Serrano, P. Santiago, G. Xiong, K. B. Ucer, and R. T. Williams, "Synthesis and optical properties of ZnO nanostructures with different morphologies," *Optical Materials*, vol. 29, no. 1, pp. 65–69, 2006, doi: 10.1016/j.optmat.2006.03.45015

Chapter 2

Experimental Procedure and Characterization Techniques

2.1 Introduction

In this study, ZnO thin films were deposited via spin coating at 3000 rpm for 30 s, followed by annealing at 240°C for 5 min. ZnO nanorods were then grown using the hydrothermal technique at 110°C for 3 hours using a 1:1 solution of zinc nitrate and HMTA. Ag nanoparticles were deposited through a photochemical reduction process involving 20% V/V solution of AgNO₃ in ethanol. The solution was drop-cast onto the sample surface, followed by UV light exposure ranging from 5 to 50 seconds to control the particle size. Metal electrodes (Ag) were deposited by thermal evaporation using a PVD system under a vacuum of $\sim 10^{-6}$ mbar. The deposition rate was maintained at 0.1–1.5 Å/s until a final thickness of 150 nm was achieved.

2.2 Material Used

2.2.1 ZnO

Zinc oxide (ZnO) is a widely studied material known for its wide bandgap (approximately 3.37 eV) and high exciton binding energy (60 meV), making it highly efficient in optoelectronic applications [45]. This wide bandgap allows ZnO to be used in ultraviolet (UV) detectors, transparent electrodes, and light-emitting devices. Its thermal stability ensures that it maintains its structural and electronic properties even at high temperatures, making it suitable for harsh environments. One of the

key advantages of ZnO is its low cost, as it is abundantly available and can be processed with economical methods, making it highly accessible for large-scale applications. In addition, ZnO is biocompatible and non-toxic, which makes it an excellent candidate for biosensing applications. Further ZnO's ability to be doped & coated with other elements enhances its electrical and optical properties, allowing for customization based on specific application needs.

2.2.2 Silver (Ag)

Silver, being a highly conductive metal, is an excellent choice for the deposition of planar electrodes onto ZnO nanostructures (NSs). With a Fermi level of 4.26 eV, silver forms an ohmic contact with ZnO, facilitating efficient charge transfer. Moreover, silver exhibits strong plasmonic effects in its nanoparticles (NPs) form [40] due to its high electrical conductivity and favorable interaction with light. This enhances light absorption, making silver nanoparticles ideal for applications that require enhanced optical properties, such as sensors, photovoltaics, and photodetectors.

2.3 Deposition Techniques

Various deposition techniques are utilized in the fabrication of photodetectors, depending on the materials and specific requirements of the device such as thermal evaporation, sputtering, chemical vapor deposition, atomic layer deposition, spin coating, dip-coating, etc. Here in this work, the spin coating technique for ZnO thin film deposition and the thermal evaporation method for metal electrode deposition have been used, which are discussed in detail here. The hydrothermal growth method for ZnO nanorods growth and the photochemical reduction method for silver NPs deposition will be discussed in the next chapter.

2.3.1 Spin coating

Spin coating is a widely utilized technique for depositing uniform thin films onto flat, clean substrates, such as glass, or onto flexible substrates like polyimide. This method allows for precise control over film thickness and uniformity, making it ideal for applications in electronics, material science, optics, and nanotechnology. In this process, a small amount of the desired liquid solution is deposited at the center of the substrate, the substrate is held tightly using a vacuum pump which is then rapidly rotated at speeds ranging from 1000 to 8000 rpm as shown in Figure 2.1. The centrifugal force generated by the spinning action spreads the liquid evenly across the surface, while excess material is removed through the edges, leaving behind a thin uniform layer. The thickness of the film is influenced by several factors, including the spin speed, spin duration, solution viscosity, and the concentration of the solute. Higher spin speeds or longer spin times generally produce thinner films, while more viscous solutions or higher solute concentrations result in thicker coatings. The

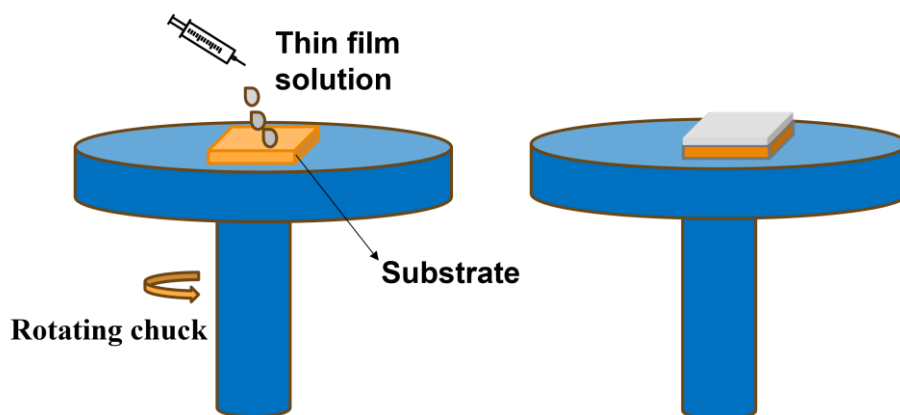


Figure 2.1: Spin coating technique

solvent in the solution evaporates during or after spinning. However, it is most effective on flat surfaces and may not provide uniform coatings on irregular substrates.

In this study, a 3M ZnO seed solution was spin-coated onto a polyimide substrate at 3000 rpm for 30 seconds to form a ZnO thin film. The coated substrate was then annealed at 240°C to improve film adhesion with the polyimide substrate.

2.3.2 Physical Vapor Deposition (PVD)

Thermal evaporation is a traditional method used for depositing metals, metal oxides, and small organic molecules onto a variety of both

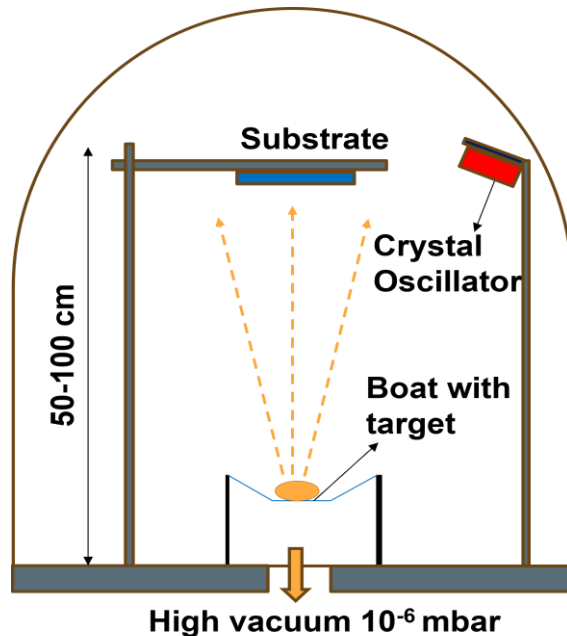


Figure 2.2: Physical Vapor Deposition Technique by thermal evaporation.

rigid and flexible substrates. The deposition process consists of two main steps: evaporation and condensation of the target material. In the first step, the target material is placed in a boat made of high-resistance materials like tungsten (W) or molybdenum (Mo). The boat is then heated to the melting point of the target material, allowing it to evaporate (see Figure 2.2). The temperature of the boat is controlled by adjusting the input electrical power. The entire process occurs under ultra-high vacuum conditions (typically between 10^{-6} and 10^{-7} mbar) to prevent the evaporated material from interacting with impurities in the air. Under such a vacuum, the mean free path of the vapor is greater than the distance between the boat and the substrate, allowing the vapor to travel to the substrate without colliding with other particles.

In the second step, the vapor condenses and deposits onto the substrate's surface. A crystal oscillator monitors the film's thickness and deposition rate. One significant advantage of physical vapor deposition

(PVD) techniques is that the evaporated material gently impacts the substrate, making it especially suitable for soft materials.

For the fabrication of a planar photodetector, interdigitated silver electrodes of thickness 150nm were deposited using a PVD system from Hind High Vacuum Private Limited, India. The initial deposition rate for silver was set at 0.1 Å/s and was gradually increased to 1-1.5 Å/s as the film thickness reached 10 nm. The schematic diagram of the thermal evaporation setup is shown in Figure 2.2.

2.4 Characterization Techniques

2.4.1 Field Emission Scanning Electron Microscope

The Field Emission Scanning Electron Microscope (FE-SEM) is a widely utilized tool in materials research, employed to investigate surface features, morphology, composition, and other properties of samples. Figure 2.3 shows the schematic of Field Emission Scanning Electron Microscope. When the electron beam strikes the sample, various electron processes occur due to the interaction between the electrons and the material. This interaction results in the emission of different types of electrons, such as secondary electrons, Auger electrons, backscattered electrons, and X-rays. Among these, secondary and backscattered electrons are primarily detected and processed to provide detailed information about the sample. Secondary electrons are produced when the incident electron beam interacts with the sample, leading to the emission of valence electrons from the surface. These electrons are highly surface-specific and are emitted from a shallow depth (less than or equal to 20 Å). Due to their low energy (less than 50 eV), secondary electrons are abundant, and their production is influenced by the accelerating voltage of the electron beam. Backscattered electrons, on the other hand, have higher energy (greater

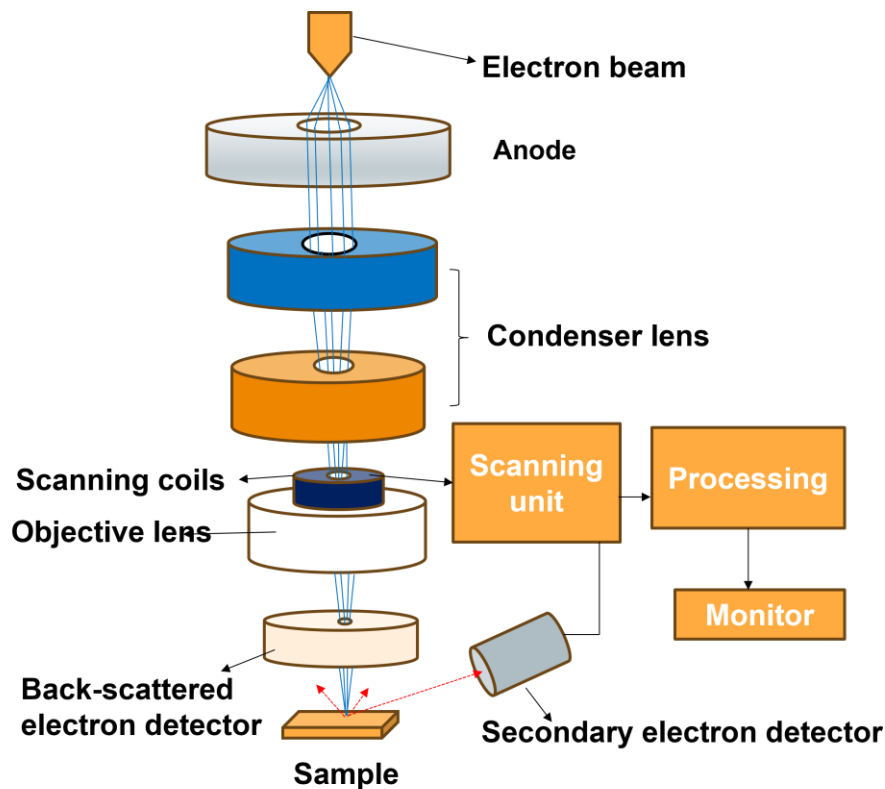


Figure 2.3: Schematic of Field Emission Scanning Electron Microscope.

than 50 eV) and are generated through elastic scattering. The yield of backscattered electrons is dependent on the atomic number (Z) of the sample, allowing for information from deeper regions within the sample to be obtained. These electrons are also sensitive to the composition of the material, which makes them useful for studying surface topography and Z -contrast.

The key components of the FE-SEM system are described below:

1. **Electron Gun:** This is the source of the incident electron beam. The energy of the electron gun typically ranges from a few hundred eV to 100 keV. In FE-SEM, electrons are emitted thermionically from a tungsten cathode and are then accelerated toward the anode. The electron emission takes place under high vacuum conditions, around 10^{-8} Torr.
2. **Condenser Lens:** Once the electron beam is generated, its diameter needs to be adjusted. This is achieved using a condenser lens, which controls the beam size by varying its

current. A lower condenser lens current results in a smaller beam diameter, offering higher resolution but potentially increasing the signal-to-noise ratio. Conversely, a larger beam diameter results in lower resolution but reduced noise.

3. **Deflection Coils:** These coils are responsible for scanning the electron beam across the sample, allowing specific regions to be examined. The digital image is formed on a computer screen by scanning the beam over the sample multiple times. Faster scanning speeds introduce more noise and lower resolution, while scanning smaller regions provides higher-resolution images within the selected window.
4. **Objective Lens:** Positioned at the lower portion of the column, the objective lens focuses the electron beam onto the sample from a short distance.
5. **Detector:** The Everhart–Thornley (ET) detector is the most commonly used detector in FE-SEM for detecting secondary electrons. It operates by using a scintillator to convert the energy of the secondary electrons into visible light photons. These photons are then detected by a photomultiplier tube (PMT), which reconverts the photons into electrons. The resulting voltage generated by the electrons in the PMT is amplified, and the corresponding electrical signal is displayed on the screen as variations in brightness.

In this work, the morphology and chemical composition of the synthesized ZnO nanostructures (NSs) and Ag-decorated ZnO nanostructures (Ag–ZnO NSs) were thoroughly investigated using a field emission scanning electron microscope (FESEM, Zeiss Supra-55) equipped with an Energy-Dispersive X-ray Spectroscopy (EDX) system. The FESEM analysis provided high-resolution surface images, enabling detailed observation of the size, shape, distribution, and vertical alignment of the pristine ZnO nanorods as well as the surface decoration by Ag nanoparticles. In the case of Ag–ZnO NSs, the presence of

uniformly dispersed Ag nanoparticles on the ZnO surface was clearly visualized, confirming successful decoration.

2.4.2 X-ray diffraction

X-ray diffraction (XRD) is a highly reliable, simple, and non-destructive technique used to determine various material properties such as crystal structure, lattice constants, crystal orientation, defects, stresses, and chemical composition. The technique utilizes incident electromagnetic radiation with wavelengths of only a few angstroms (typically between 0.7 and 2 Å), which is comparable to the spacing between lattice planes.

For thin films or powdered samples, a monochromatic X-ray beam is directed at the sample, and a detector is positioned at an angle relative to the incident beam as shown in Figure 2.4. Various metals, such as Cu, Co, Mo, and Cr, can be used as cathodes for X-ray generation. In our study, copper (Cu) was chosen as the X-ray source due to its wavelength being close to the lattice parameters of ZnO, ease of cooling, and the availability of standard data. The incident angle (2θ) generally varies from 20° to 80° , and the intensity of the diffracted X-rays is measured by the detector to generate a diffraction intensity plot across different angles. Diffraction peaks occur when constructive interference is achieved between the reflected X-rays, which is governed by Bragg's law:

$$n\lambda = 2d \sin\theta_b \quad (2.1)$$

Where:

- n is the order of diffraction,
- λ is the X-ray wavelength,
- d is the distance between atomic planes, and
- θ_b is the angle between the X-ray and the crystal planes.

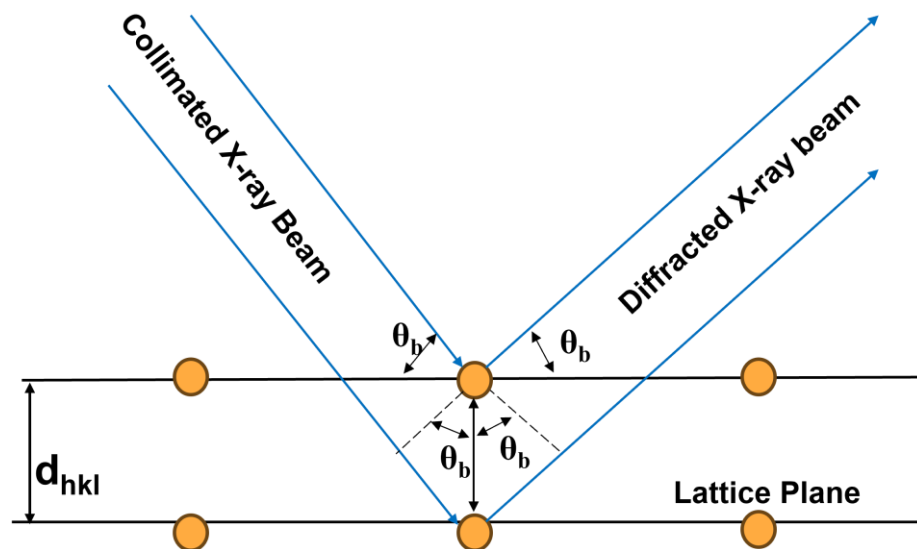


Figure 2.4: Schematic diagram of Bragg's law.

The relative intensity of these diffraction peaks is influenced by the type and arrangement of atoms in the crystal. By comparing the observed peak positions with standard JCPDS data files, valuable insights about the crystal lattice can be obtained, such as peak shifts or broadening, which indicate structural variations.

In this work, X-ray diffraction (XRD) analysis of Ag-decorated ZnO nanorod arrays was performed using a Rigaku D/Max-2000 PC diffractometer with $\text{CuK}\alpha$ radiation ($\lambda = 1.54056 \text{ \AA}$) at an operating voltage of 40 kV. Diffraction patterns were recorded over a 2θ range of 20° to 80° , using a scanning rate of 2° per minute. The XRD measurements were used to investigate the crystalline structure, phase composition, and possible structural modifications induced by the decoration of ZnO nanorods with silver nanoparticles. The characteristic diffraction peaks corresponding to the hexagonal wurtzite structure of ZnO were identified, and additional peaks related to the face-centered cubic (fcc) structure of metallic silver confirmed the successful decoration. Furthermore, changes in peak intensity and broadening were analyzed to assess the influence of Ag incorporation on crystallite size, lattice strain, and preferred orientation of the ZnO nanorods.

2.4.3 UV-Visible Spectroscopy

When electromagnetic waves interact with a material, various phenomena can occur, such as scattering, reflection, transmission, absorption, and fluorescence/phosphorescence. Absorption happens when the photon energy of the incident light is equal to or greater than the bandgap of the material. Figure 2.5 illustrates the operation of a typical UV-Vis spectrophotometer. When light strikes a sample, it either transmits through or is absorbed by the sample. The amount of light absorbed can be determined by calculating the difference between the intensity of the incident light (I_0) and the transmitted light (I). Absorbance denoted as A , can be quantified using the equation

$$A = -\log(T) = -\log(I/I_0) \quad (2.2)$$

In this equation, A is the absorbance, T is the transmittance, and I_0 and I are the intensities of the incident and transmitted light at a specific wavelength, respectively. Absorbance is a dimensionless quantity. A typical UV-Vis spectrophotometer consists of a broadband light source, such as a tungsten-halogen or deuterium lamp, a dispersive element for separating different wavelengths, and a detector that converts light intensity into an electrical signal. Initially, the absorption of the bare substrate is measured as a baseline, which is then subtracted from the sample data to isolate the absorption characteristics of the sample itself.

The monochromatic light from the dispersive element is split by a beam splitter, directing one beam onto the sample and the other onto a reference cell. The transmitted light through both the sample and the reference cell is detected and recorded. The absorption spectrum of thin films is obtained by subtracting the reference spectrum from the substrate spectrum. The absorption of materials also depends on the thickness of the sample, as described by the Beer-Lambert law:

$$I(\lambda) = I_0 \times e^{-\lambda \alpha d} \quad (2.3)$$

where I_0 is the incident light intensity, α is the absorption coefficient, and d is the thickness of the sample.

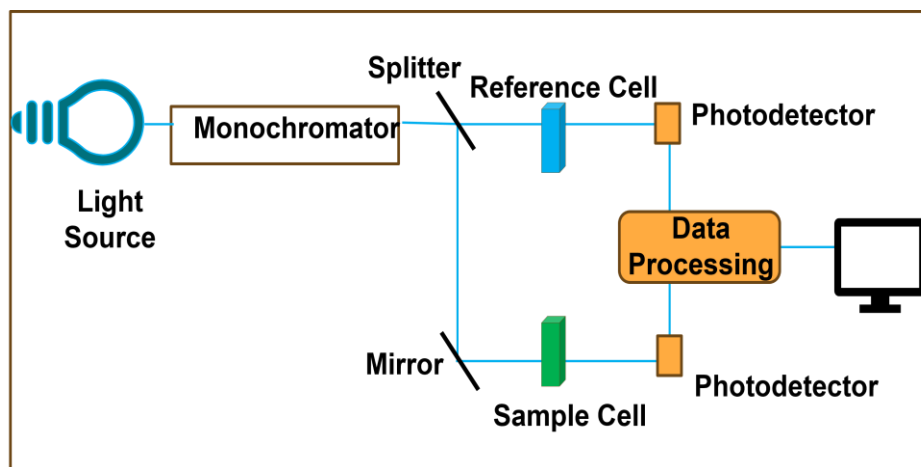


Figure 2.5: Schematic diagram of UV-visible spectrometer.

All absorption spectra presented in this thesis were measured using a Perkin Elmer Lambda 365+ UV-Visible spectrophotometer. UV-Visible absorption measurements were carried out in the wavelength range of 300–800 nm in normal incidence mode for both pristine ZnO nanorod arrays (ZnO NRAs) and silver-decorated ZnO nanorod arrays (Ag–ZnO NRAs) grown on glass substrates. Cleaned glass substrates were used as reference baselines to eliminate background absorption and isolate the contribution of the nanostructured films. This technique was employed to evaluate the optical absorption characteristics and to analyze the influence of Ag nanoparticle decoration on the light-harvesting capabilities of the ZnO NRAs. The measurements provide critical information about the absorption edge, optical transitions, and photon interaction behavior within the nanostructures. The comparison between pristine and Ag-decorated ZnO NRAs helped reveal the role of localized surface plasmon resonance (LSPR) effects and hot electron generation in enhancing optical absorption in the UV-visible range.

2.4.4 Photoluminescence Spectroscopy

Luminescence refers to the spontaneous emission of light that occurs when a material absorbs energy. In semiconductors, this process

is triggered when a laser with optical energy greater than the material's bandgap strikes the surface, promoting electrons from the valence band to the conduction band. These excited electrons eventually return to the valence band by recombining with holes. Recombination can occur via two pathways: radiative recombination, where the energy is released as photons, contributing to the material's luminescence, or non-radiative recombination, where energy is lost as heat. Only radiative recombination produces photon emission, making it central to the material's luminescence properties.

For high quantum efficiency, the non-radiative lifetime should be significantly larger, indicating a lower probability of non-radiative recombination. Impurities in the material can introduce mid-gap states, allowing electrons to recombine through these states, leading to the emission of lower-energy photons. This emission provides qualitative information about the density of mid-gap states present in the sample.

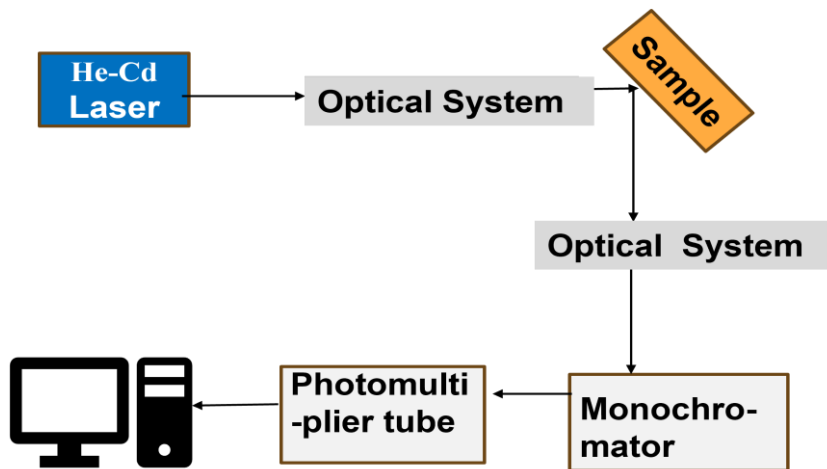


Figure 2.6: Schematic of PL measurement setup

In this study, photoluminescence (PL) measurements were carried out to investigate the optical emission characteristics of pristine ZnO nanorod arrays (ZnO NRAs) and Ag-decorated ZnO nanorod arrays (Ag-ZnO NRAs). The measurements were performed using a Dongwoo Optron PL system, employing a He-Cd laser with an excitation wavelength of 325 nm. All PL spectra were recorded at room

temperature. A schematic diagram of the PL measurement setup is presented in Figure 2.6.

PL spectroscopy was utilized to probe the electronic structure, defect states, and recombination dynamics within the nanostructures. Specifically, it enabled the identification of near-band-edge (NBE) emissions associated with excitonic recombination, as well as deep-level emissions (DLE) arising from intrinsic defects such as oxygen vacancies or zinc interstitials. By comparing the PL spectra of pristine and Ag-decorated ZnO NRAs, the effect of Ag nanoparticles on the recombination processes and surface defect passivation could be assessed.

2.4.5 Current-Voltage (I-V) Characterization

I-V characterization is a crucial technique for evaluating the performance of electronic devices. In this study, we conducted electrical measurements on ZnO nanostructure-based MSM photodetectors. All I-V measurements were performed using a Keithley 2612 source meter. The current was recorded both at a constant applied bias and during a voltage sweep from negative to positive values. The I-V characteristics were measured under dark conditions as well as under light illumination, with wavelengths ranging from 250 nm to 800 nm.

To measure device performance the following performance parameters are calculated:

- 1. Dark Current (I_d):** Dark current in UV photodetectors refers to the small electrical current that flows through the device even in the absence of light. This current is primarily generated due to thermal excitation of charge carriers (electrons and holes) within the material, or defects and impurities in the semiconductor. Dark current is an unwanted signal, often considered as noise, and it can severely impact the photodetector's performance, particularly when detecting weak UV signals

2. **Photo-current (I_{ph}):** Photocurrent in UV photodetectors is the current generated when the device absorbs ultraviolet (UV) light and converts it into an electrical signal. When UV photons hit the active material of the photodetector, they excite electrons from the valence band to the conduction band, creating electron-hole pairs. These charge carriers are then separated and collected under the influence of an external electric field, resulting in a flow of current known as photocurrent.
3. **Response Time and Recovery Time:** Response time and recovery time are key performance parameters in UV photodetectors, particularly for applications that demand rapid detection of varying light intensities, such as in communication systems, high-speed imaging, or pulsed UV light measurements. The response time refers to the period it takes for the photodetector to respond to an increase in UV light intensity, specifically the time it takes for the photocurrent to rise from 10% to 90% of its maximum value. Similarly, recovery time is the period the device takes to return to its baseline state after the UV light source is turned off, specifically how long it takes for the photocurrent to drop back to 10% of its maximum value. Both response and recovery times are critical for determining the overall speed and accuracy of UV photodetectors, with shorter times ensuring better performance in high-speed and time-sensitive applications.
4. **Sensitivity (S):** Sensitivity represents the photodetector's ability to detect low levels of light, and it is influenced by factors such as dark current, responsivity, and noise

$$S = \frac{I_{ph}}{I_d} \quad (2.4)$$

5. **Responsivity (R):** It is a key performance metric for UV photodetectors, representing the efficiency with which the device converts incident ultraviolet (UV) light into an electrical signal. It is defined as the ratio of the photocurrent generated by the detector to the power of the incident light and is typically measured in amperes per watt (A/W). Essentially, responsivity indicates how much

current the photodetector produces for a given amount of incoming UV light, making it a direct measure of the device's sensitivity to UV radiation.

$$R = \frac{\Delta I}{P_o} \quad (2.5)$$

here, ΔI is $I_{ph} - I_d$, and P_o is the optical power.

6. **Specific detectivity (D^*):** It is a key figure of merit used to quantify the performance of photodetectors, including UV detectors. It measures the detector's ability to sense weak signals. It is defined as the reciprocal of the noise-equivalent power (NEP), normalized by the active area of the detector and the bandwidth of the measurement. The formula for specific detectivity is given by:

$$D^* = R \sqrt{\frac{A_o}{2eI_d}} \quad (2.6)$$

where R is the responsivity of the device, A_o is the device's active area, e is the absolute charge on an electron, and I_d is dark current.

7. **External Quantum Efficiency (EQE):** External quantum efficiency is the number of charge carriers generated by a single photon. It is given by the following equation:

$$EQE = \frac{hcR}{e\lambda} \quad (2.7)$$

Where h , c , R , e , and λ represent Planck's constant, the speed of light, photoresponsivity, the elementary charge of an electron, and the wavelength of the incoming light, respectively.

Chapter 3

Silver Nanoparticle Decorated ZnO Nanorod Array Based Highly Sensitive Photodetector

This chapter focuses on the development of a solution-processed high-sensitivity & flexible UV photodetector. It utilizes hydrothermally grown ZnO nanorods decorated with photochemically deposited Ag nanoparticles to achieve high photosensitivity & photoselectivity of UV-A light.

3.1 Introduction

ZnO-based UV photodetectors are highly desired for various applications viz. biomedical, defense, and communications. Many other metal oxide semiconductor-based wide bandgap materials have gathered attention such as NiO, ZnO, CuO, In₂O₃, ZnCr₂O₄, and SnO₂. [1-6]. Among all, ZnO has been used extensively due to its cost-effectiveness, high carrier mobility, biocompatibility, high chemical & thermal stability, non-toxicity, and the ability to form various morphologies of nanostructure, developed using the hydrothermal technique. Nanostructures, with their high surface area-to-volume ratio, can significantly enhance absorption, ultimately boosting the sensitivity and responsivity of the device. Various fabrication methods have been effectively used to produce these nanostructures, including pulsed laser deposition (PLD) [7], RF-magnetron sputtering [8], chemical vapor deposition (CVD) [9], and the hydrothermal technique [10]. However, PLD, CVD, and sputtering are considerably more expensive and complex due to the high cost of materials and the need for advanced equipment to maintain precise growth conditions. In this work, we

utilized the hydrothermal technique, due to its advantages such as low fabrication cost, less complexity, and requirement of low-temperature processing conditions (80-150°C). Using 1mM KMnO_4 as an additive enhances the crystallinity of the ZnO NRs, reduces defects and promotes their preferred orientation along the c-axis [43] Chapter 1.

Also, in the past, researchers have deposited metal nanoparticles such as silver (Ag) onto the ZnO Nanostructure (NSs) and demonstrated plasmonic coupling between them, to enhance various performance parameters such as photosensitivity, responsivity, response speed, etc. [29]. Further research is still needed to optimize the size of silver nanoparticles, in order to maximize the plasmonic coupling effect between Ag-NPs and ZnO NRs. Also, previous research has focused on various methods for integrating ZnO nanostructures with metal nanoparticles such as thermal evaporation [12], sputtering [13], and solution processing techniques [14]. Among them, the photochemical reduction (PCR) method (a solution-processed technique) offers simplicity, cost-effectiveness, and scalability. However, obtaining enhanced performance parameters such as high photosensitivity, responsivity, selectivity, stability, affordability, and flexibility of the device, all at once, remains a challenge.

In this work, the ZnO nanorod arrays (NRA) were deposited via the hydrothermal technique over functionalized and precleaned polyimide substrates. KMnO_4 was used as an additive in the precursor solution of the hydrothermal method. Later, these ZnO nanorod arrays (NRA) were capped with silver nanoparticles (Ag-NPs) using the photochemical reduction (PCR) technique. By suitably varying the UV light illumination time in the photochemical reduction process, the sizes of the silver nanoparticles were effectively controlled. The plasmonic effects of silver NPs were optimized by varying the sizes of silver NPs, deposited on the ZnO NSs to enhance various performance parameters such as sensitivity, selectivity, responsivity, and switching response speed. Further to increase the flexibility of the device, polyimide as a substrate was used. The proposed device shows promise for UV sensor-based photodetector applications, where high sensitivity, selectivity,

responsivity, and response speed are of utmost importance and making it promising for applications in wearable health monitoring (such as UV exposure detection), environmental sensing (including radiation assessment), and biomedical diagnostics (like skin cancer screening).

3.2 Experimental Details

The fabrication of the Ag-ZnO nanorod-based flexible UV photodetector involved a multi-step process comprising substrate cleaning, seed layer deposition, nanorod growth, silver nanoparticle decoration, and electrode deposition, as outlined in Figure 3.2. A 1.5 cm × 1.5 cm polyimide sheet served as the flexible substrate. Initially, the substrate was sequentially cleaned in acetone, isopropanol (propan-2-ol), and deionized (DI) water using ultrasonication for 15 minutes each to remove organic and particulate contaminants. To enhance hydrophilicity and improve adhesion of the subsequent ZnO seed layer, the substrate was subjected to a surface activation treatment using a mixture of liquid ammonia, hydrogen peroxide, and DI water in a 1:1:5 volume ratio at 60°C for 15 minutes.

For seed layer preparation, a 3M zinc acetate solution was formulated using ethanolamine as the stabilizer and 2-methoxyethanol as the solvent. The solution was stirred at 380 rpm for 6 hours to ensure homogeneity. The prepared seed solution was then spin-coated onto the pretreated polyimide substrate at 3000 rpm for 30 seconds. After spin-coating, the sample was annealed at 240°C for 5 minutes in a thermal oven to improve film crystallinity and adhesion to the substrate.

Growth of ZnO nanorods was achieved via a hydrothermal method. A precursor solution containing 0.1 M zinc nitrate and 0.1 M hexamethylenetetramine (HMTA) was prepared in DI water. To promote vertical alignment and suppress lateral growth, 1 mM potassium permanganate (KMnO₄) was added as an oxidizing agent. The seeded substrates were immersed in the solution, sealed inside a glass beaker, and kept in a thermal oven at 110°C for 3 hours. Post-growth, the

samples were thoroughly rinsed with DI water to remove residual salts and dried under ambient conditions.

Silver nanoparticles (Ag-NPs) were then deposited on the ZnO nanorods via a photochemical reduction (PCR) method, chosen for its low-temperature, solution-processed compatibility with flexible substrates. A 20% V/V solution of silver nitrate in ethanol was prepared and stirred for 15 minutes to ensure proper dissolution. This solution was drop-cast onto the ZnO nanorod arrays, followed by UV irradiation using a 254 nm, 11-watt UV lamp for varying durations of 5, 10, 20, and 50 seconds to control nanoparticle size as illustrated in Figure 3.2. During UV exposure, electrons from ZnO's conduction band reduced Ag^+ ions to metallic Ag, while ethanol acted as a hole scavenger by forming aldehydes. After deposition, the samples were rinsed with DI water to remove reaction byproducts and then dried under ambient conditions for 2 hours respectively.

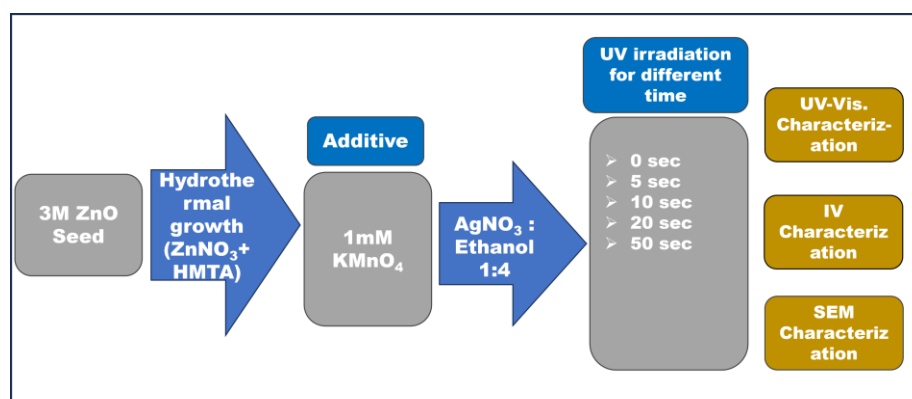


Figure 3.1: Experimental Plan

Finally, for, the optoelectronic characterization, the silver IDE electrodes of 154nm thickness were deposited using a shadow mask and a physical vapor deposition technique at a rate of 0.1 Å/s under a vacuum of 5×10^{-6} mbar. The morphology and chemical composition of the NSs were analyzed using a Zeiss Supra-55 Field Emission Scanning Electron Microscope and energy-dispersive X-ray. Photoluminescence properties were examined with a Dongwoo Optron DM 500i photoluminescence analyzer, which used a He-Cd laser with a 325 nm wavelength as an excitation source and a PMT detector. Additionally, absorption spectra

were obtained using a UV-Vis spectrophotometer (Perkin Elmer lambda365+) & I-V characterization were done using Keithley 2612A source meter.

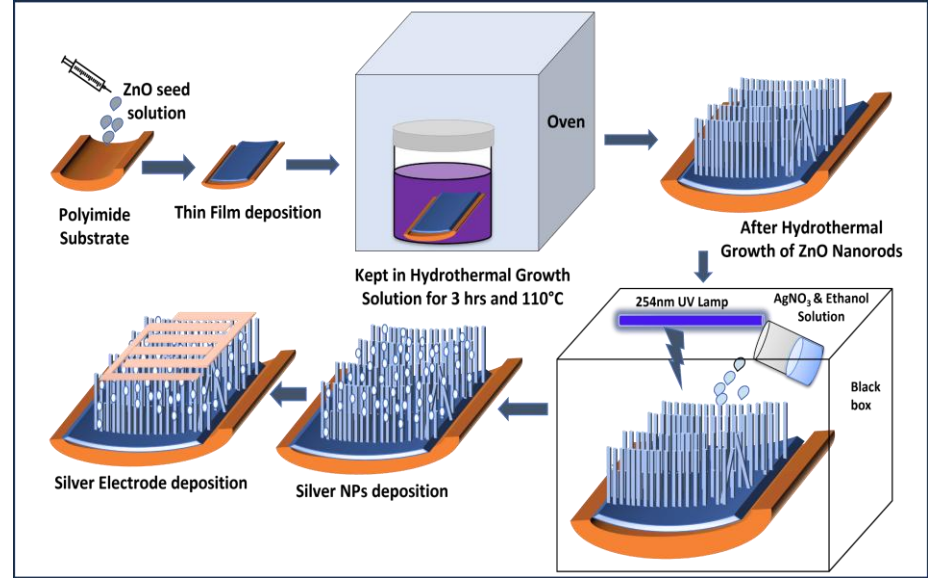
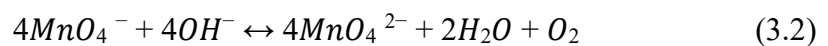
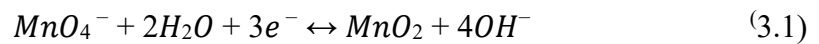


Figure 3.2: Experimental procedure schematic

3.3 Results and Discussions

3.3.1 Growth of ZnO nanorods:

In Chapter 1, the growth mechanism of pristine ZnO nanorods using the hydrothermal method has already been described. Here, we will focus on the mechanism for producing highly oriented ZnO nanorods by introducing KMnO_4 as an additive into the precursor solution. KMnO_4 , a well-known oxidizing agent, plays a dual role in the solution. First, it facilitates the generation of OH^- ions, which are responsible for the increased diameter of the ZnO nanorods. Secondly, it releases O_2 , and the alignment of the ZnO nanorods is largely determined by the oxygen levels in the solution. The chemical reactions involved in this process are outlined below:



Moreover, ZnO inherently shows anisotropic growth because of the alternating O^{2-} and Zn^{2+} planes in its wurtzite crystal structure, which is the most thermodynamically stable form at room temperature. The presence of $KMnO_4$ increases the oxygen concentration in the solution during the growth process, thereby promoting vertical growth even further.

3.3.2 Deposition of silver nanoparticle:

As shown in Figure 3.3, silver (Ag) nanoparticles (NPs) were deposited on ZnO nanorods (NRs) using the photochemical reduction technique. Firstly, a 20% V/V solution of silver nitrate in ethanol was dissolved and stirred in a beaker for 10 min. Then, the solution was

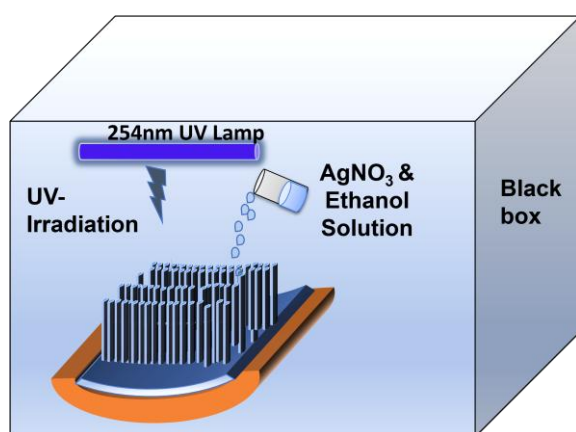


Figure 3.3: Schematic of Ag nanoparticles deposition

dispersed onto the ZnO NRs sample, and placed under UV illumination inside a black box, with varying illumination time duration. A 254 nm 11 W Phillips UV lamp was used for UV light illumination. Finally, after the deposition of silver-NPs, the samples were rinsed thoroughly in DI water, to remove the byproducts and subsequently annealed at 180° C for 10 min. The growth mechanism for Ag-NPs deposition can be explained as follows, the ZnO nanostructures (NSs) are illuminated with UV light for the generation of electron-hole pairs inside ZnO (NSs). Electrons of the conduction band (CB) of ZnO NSs are captured by the silver ion, reducing the silver ions to form silver atoms on the ZnO NSs surface. Ethanol will act as a hole scavenger and will be oxidized to

ethanal by capturing the holes from the ZnO Valence band (VB). As the UV illumination time increases, a greater number of silver ions are reduced on the surface of the ZnO nanorods, resulting in the formation of larger or agglomerated silver nanoparticles as shown in Figure 3.4. The size of silver-NPs, thus can be effectively controlled by suitably varying the UV illumination time. Nitric acid & ethanal are the byproducts obtained in the reaction [16].

The reaction mechanism is given below:

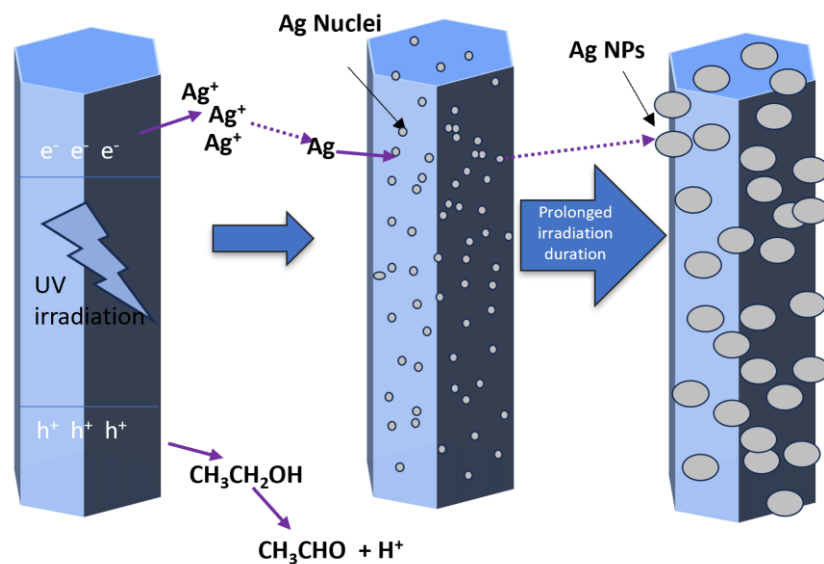
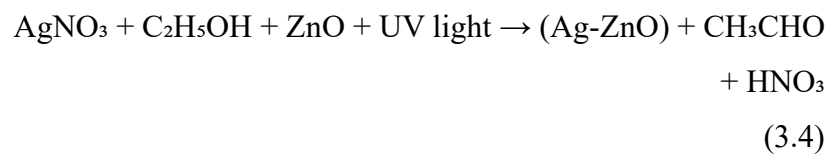
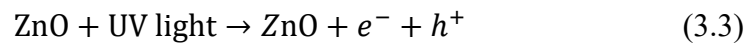


Figure 3.4: Ag nanoparticle deposition mechanism

3.3.3 Optical Characterization:

Five different samples and devices were prepared with silver deposition times of 0, 5, 10, 20, and 50 seconds, achieved by controlling the UV illumination exposure time. Each sample was subsequently characterized and will be referred to accordingly as S0, S5, S10, S20, and S50. FESEM images were taken to observe the morphologies of pristine ZnO nanorods (NRs) and silver (Ag) deposited ZnO NRs. From

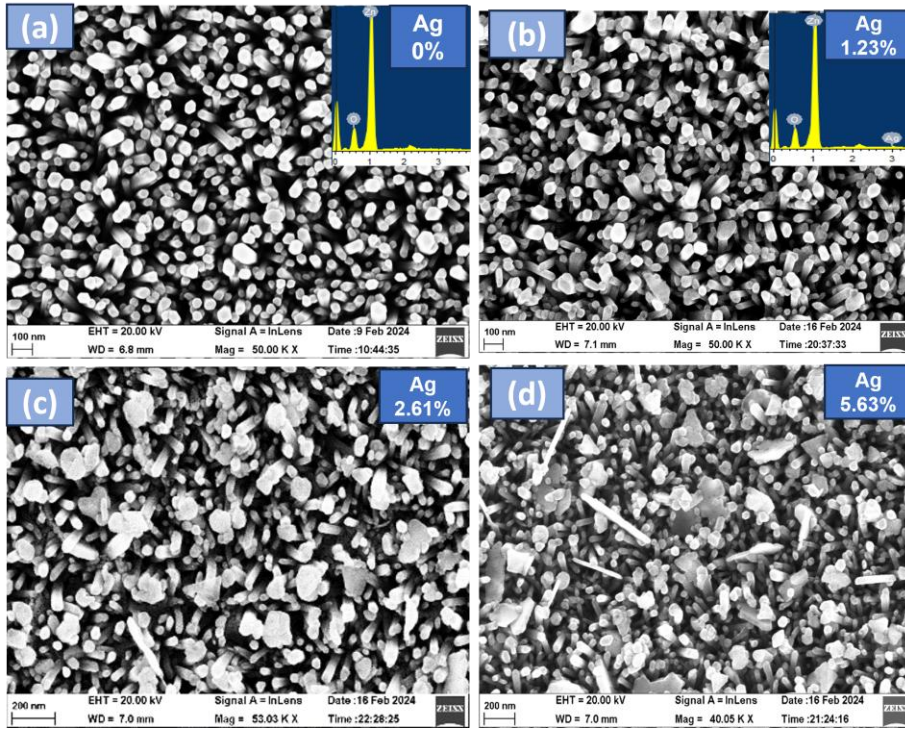


Figure 3.5: FESEM image of a) S0 sample (pristine ZnO), the inset shows it's EDS spectra b) S5 sample (Ag-ZnO), the inset shows EDS spectra c) S20 sample (Ag-ZnO) d) S50 sample (Ag-ZnO).

Figure 3.5 a) of pristine ZnO NRs, we can infer that highly dense & uniformly distributed ZnO NRs have been obtained with average length & diameter of 520 nm and 30 nm respectively.

As silver is deposited onto the pristine ZnO NRs array, the FESEM images reveal changes in the surface morphology. With increasing the silver deposition time from 5 sec to 50 sec (as seen in Figure 3.5 (b,c,d)), there is a noticeable change in the texture and aggregation of the particles, indicating that silver nanoparticles are forming on or within the ZnO NRs array. However, for the S5 sample (with 1.63% EDX silver content), there are not many noticeable changes which can be attributed to the very small size of silver NPs lying in the range of (0 to 30 nm).

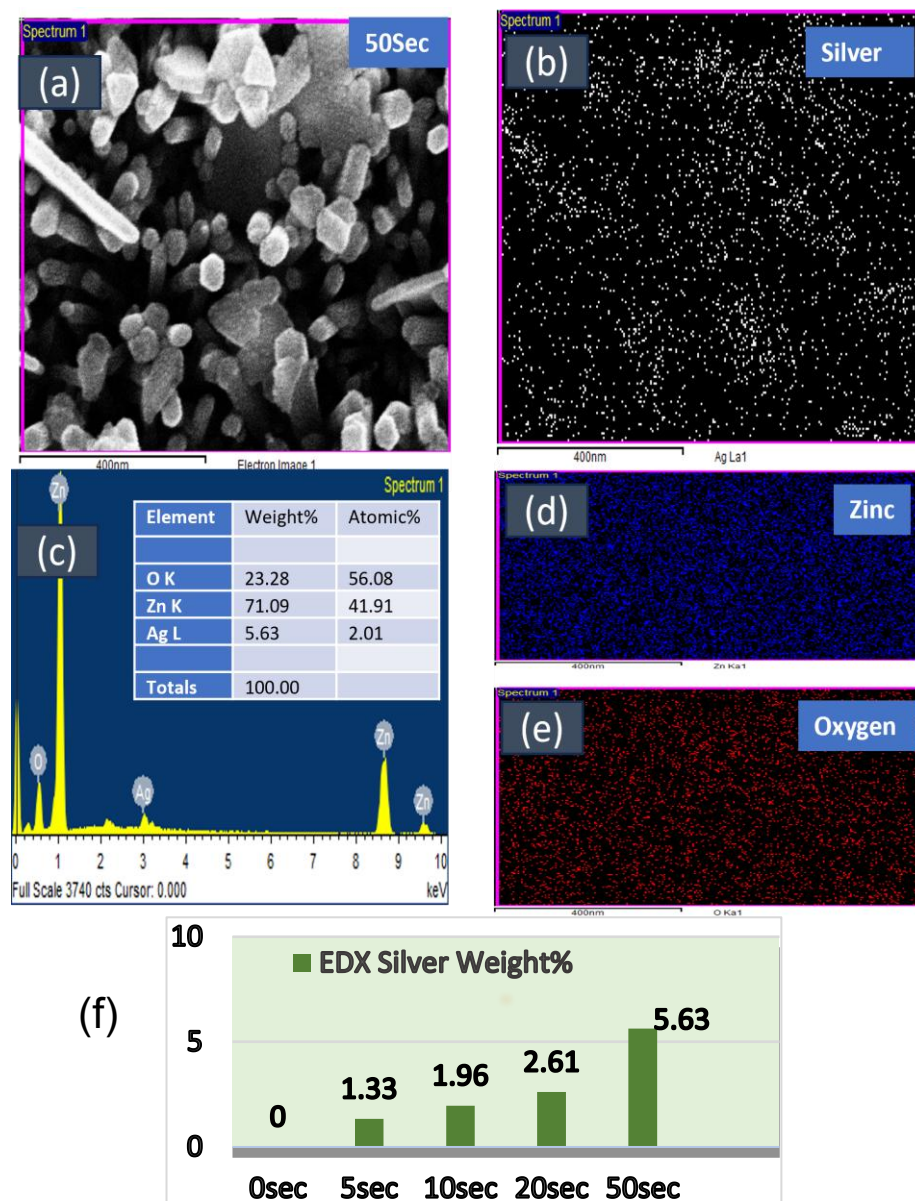


Figure 3.6: a) FESEM image of S50 sample b) Elemental mapping of silver c) Edx spectra & elements weight % d) Elemental mapping of Zinc e) Elemental mapping of oxygen f) Edx silver weight % vs silver deposition time.

Also, From Figure 3.6, EDX confirmed the presence of silver NPs deposition because as the deposition time increases from 5 sec to 50 sec the EDX result shows a progressive increase in silver content. For example, the silver content increases from 1.33% after 5 seconds to 5.63% after 50 seconds of silver deposition.

Energy Dispersive X-ray Spectroscopy mapping was employed to assess the spatial distribution of Ag on ZnO nanorods. The results indicated a uniform dispersion of Ag nanoparticles for samples exposed to UV light for 5–10 sec. At 50 sec exposures, agglomeration became apparent, leading to heterogeneous particle clusters that negatively impacted photocurrent. FESEM images and elemental maps further supported these observations. Figure 3.6(b) was added to visually illustrate the EDX mapping results, and the text correlates these distribution patterns with variations in device responsivity.

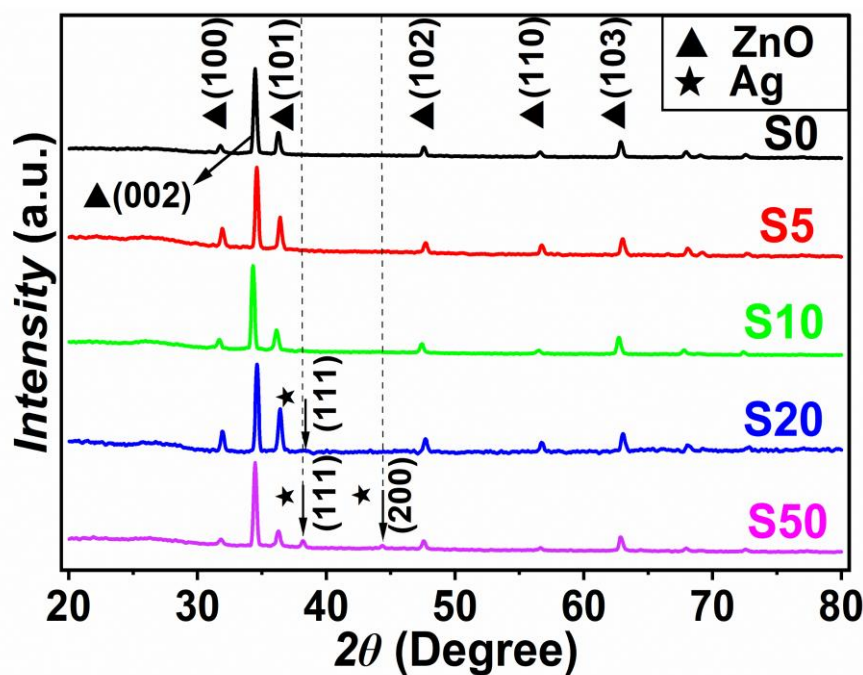


Figure 3.7: XRD plots for all the samples

X-ray diffraction (XRD) is the method for the characterization of the crystalline structure of ZnO and Ag-ZnO NSs. From Figure 3.7 the peaks from the XRD plot indicate that ZnO has a hexagonal wurtzite structure, which includes planes such as (100), (002), and (101) were in good agreement with the JCPDS file of ZnO (JCPDS file no. 36-1451) [17]. A higher intensity of peak was obtained for the (002) plane, indicating more crystallinity along the polar c-axis. These planes are essential for determining the anisotropic properties and orientation of the material. The prominent (111) and (200) diffraction peaks of silver observed at 38.1°, and 44.3° in the plot for S50 and at 38.1° for S20

samples suggest the face-centered cubic (FCC) structure of the silver (JCPDS file no. 04-0783 [17]) has been deposited on the surface of the ZnO, confirming that silver nanoparticles were successfully deposited on the surface of ZnO. As the time of silver deposition increases, the intensity of these Ag peaks also increases, which means that silver is becoming more crystallized and concentrated.

Figure 3.8 shows the UV–Visible absorption spectra of pristine ZnO (S0) and Ag-decorated ZnO nanorods (S5, S10, S20, and S50). A clear variation is observed in the spectral behavior across both UV and visible regions with increasing Ag nanoparticle (Ag-NPs) deposition time. Pristine ZnO displays a single sharp absorption edge in the UV region, corresponding to its fundamental bandgap transition. However, upon deposition of Ag-NPs, the absorption profile significantly changes, particularly for the S5 and S10 samples, which exhibit distinct enhancements in the UV region with the emergence of multiple peaks. This increase in absorption for S5 and S10 samples can be attributed to the localized surface plasmon resonance (LSPR) effect arising from smaller-sized Ag-NPs. These smaller Ag-NPs effectively interact with incident UV light by transferring maximum energy to oscillating electrons. This enhances absorption and contributes to improved carrier generation [18].

In contrast, for samples treated with longer UV illumination times (S20 and S50), where Ag-NPs grow larger due to agglomeration, the absorption in the UV region declines relative to pristine ZnO. This is primarily due to a reduction in LSPR efficiency as larger Ag-NPs transition from absorption-dominant to scattering-dominant behavior. As the particle size becomes comparable to or larger than the incident UV wavelength, radiative decay (i.e., scattering losses) [19] increases, reducing net absorption [18]. Additionally, large Ag-NPs tend to block active absorption sites on ZnO nanorods, further reducing UV light penetration and photocurrent generation efficiency.

In the visible region, all Ag-decorated ZnO samples exhibit significantly higher absorption compared to pristine ZnO, which remains nearly transparent due to its wide bandgap. This enhancement

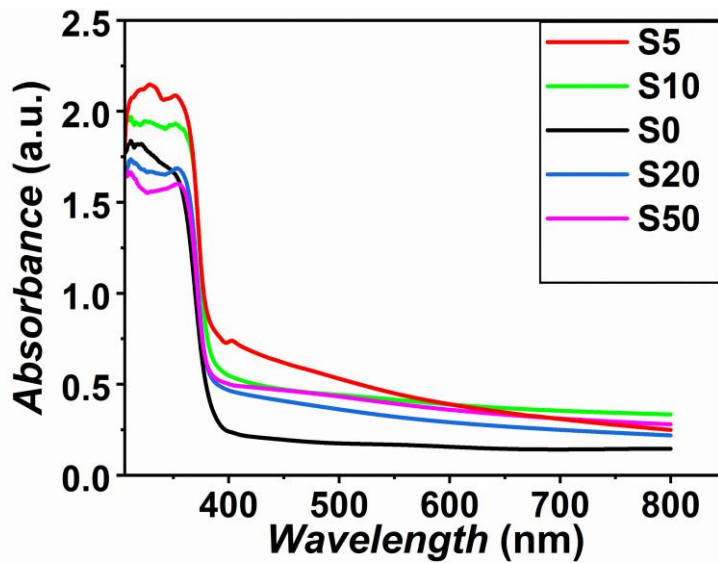


Figure 3.8: UV-Vis's absorption spectra of pristine ZnO and Ag-ZnO NRs

is most prominent in the S5 and S10 samples, where smaller Ag nanoparticles contribute more effectively to light absorption through localized surface plasmon resonance (LSPR). Notably, in the S5 sample, a distinct peak (at 410 nm) appears in the visible range, corresponding to the LSPR frequency of the smaller-sized Ag-NPs, indicating strong plasmonic activity. In contrast, the multiple peak in UV absorption observed in the S5, S10, S20 and S50 samples arises from interparticle plasmonic coupling and the emergence of multipolar resonance modes [16].

In Figure 3.9, the Tauc plot has exhibited a significant decrease in the bandgap after the deposition of Ag-NPs, which could be due to the enhancement of absorption of light in the visible region and could be attributed to the reverse of the Burstein-Moss effect UV- vis spectra of pristine ZnO and Ag-ZnO NSs [16].

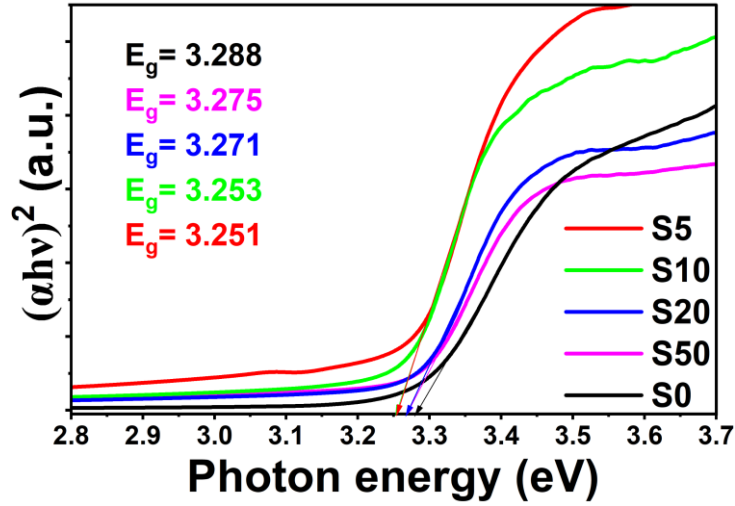


Figure 3.9: Tauc plot of pristine ZnO and Ag-ZnO NRs

Photoluminescence (PL) is used to study defects in ZnO. In the ultraviolet (UV) region, the peak is due to the band-to-band edge transfer, while in the visible region, it is due to intrinsic defects. In Figure 3.10, The PL intensity increases for the defects-level emission (DLE) and near-band edge (NBE) emission for the S5 and S10 samples. However, it decreases in both cases for the S50 sample compared to pristine ZnO. The increase in PL emission for the S5 and S10 samples is attributed to the strong plasmonic coupling effect in the smaller-sized Ag-NPs. This effect generates highly energetic hot electrons within the Ag-NPs, which are subsequently transferred to the conduction band and defect levels of ZnO for Fermi-level alignment [21]. These transferred electrons then fall back to the valence band and defects level of ZnO, leading to the enhancement of both NBE and DLE as shown in Fig. 4(a). The PL emission in the visible region may also increase due to lattice mismatch defects, present at the Ag-ZnO interface. However, for the S50 sample, the decrease in PL emission (both DLE & NBE emission) is attributed to the quenching effect by Ag-NPs. Larger Ag-NPs exhibit a weaker plasmonic coupling effect due to their weak absorption, which is insufficient to generate highly energetic hot electrons. Hence, for Fermi-level alignment, the ZnO CB electrons will be captured by the Ag-NPs, leading to a reduction in electron density inside the ZnO CB (which is the reverse of the earlier case). The deficient electrons

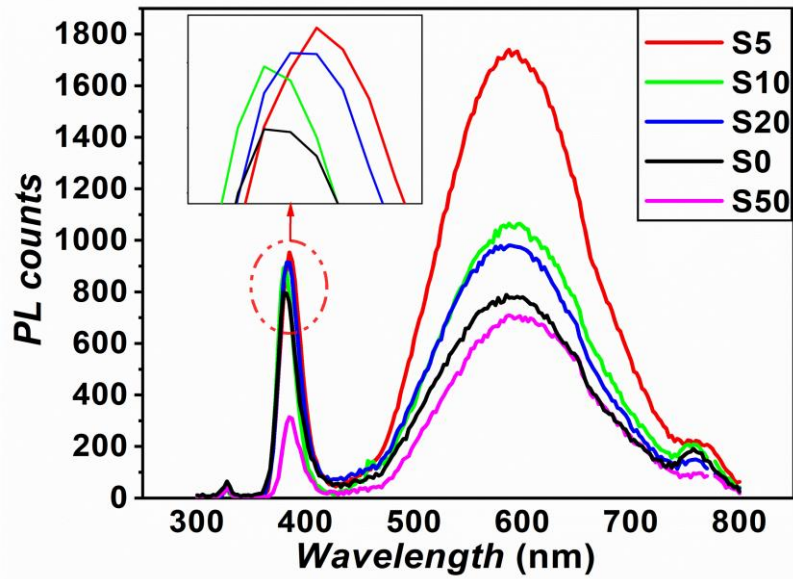


Figure 3.10: Photoluminescence spectra of pristine ZnO and Ag-ZnO NRs

recombine with the valence band and defect levels, resulting in a decrease in near-band-edge (NBE) and defect-level emissions (DLE) compared to pristine ZnO, as shown in Figure. 3.14.

3.3.4 Electrical characterization:

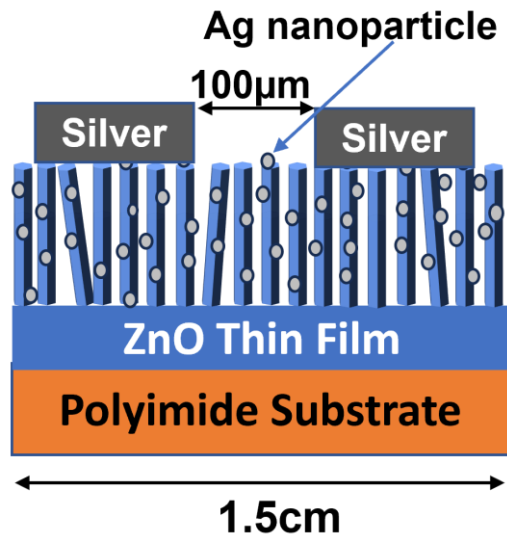


Figure 3.11: Device Structure Ag-ZnO

Figure 3.11, depicts an MSM device configuration with interdigitated silver electrodes of a channel length of 100 μm and a channel width of 55 mm. A light source of 0.8mW/cm² optical power

with 250 nm to 800 nm wavelength range has been used to illuminate the devices. The I-V characterization of the devices at an applied sweep voltage from -20 to 20 V is shown in Figure 3.13. The device based on Ag-ZnO exhibited highly selective photoresponse to UV-A radiations, with peak photoresponsivity at 330 nm. From Figure 3.12, Photosensitivity (S) obtained was highest at 4.21×10^7 for the S5 device and lowest at 1.01×10^3 for the S50 device, as compared to pristine ZnO at 7.91×10^4 . Photoresponsivity ($R = I_{\text{photo}}/P_o$) of the Ag-ZnO-based device obtained, was highest at 31.79 A/W for the S5 device, lowest at 0.014 A/W for the S50 device, and 0.24 A/W for the pristine ZnO device, where I_{photo} is photocurrent and P_o is optical intensity of incident light.

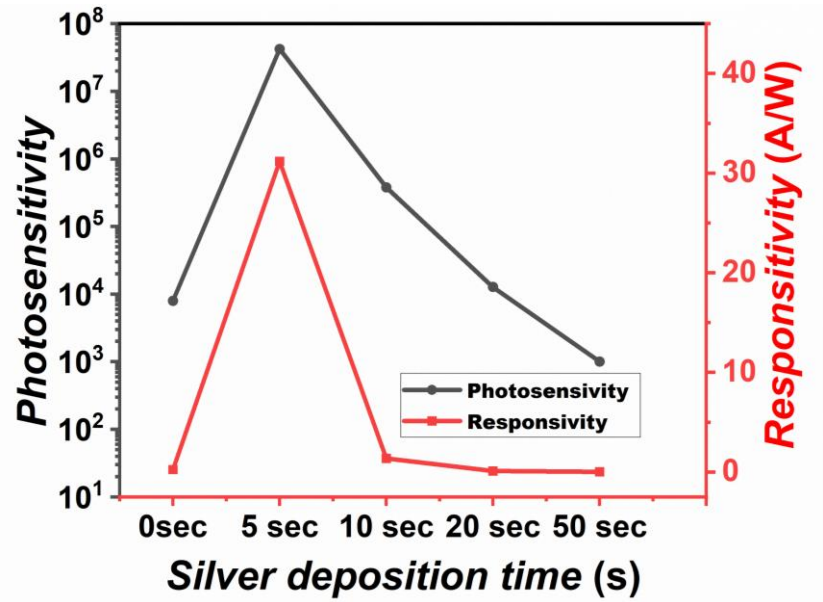


Figure 3.12: Photosensitivity & responsivity vs. silver deposition time.

The UV to visible rejection ratio at ($R_{(330\text{nm})}/R_{(450\text{nm})}$) has also increased from 3.23×10^3 to 1.75×10^4 for S5 device compared to pristine ZnO. All these performance parameters were calculated against a wavelength of 330 nm and at 20 V applied voltage bias. From Figure 3.13, we can infer that after the deposition of the silver nanoparticle, the dark current (I_d) has been reduced for all Ag-deposited devices, also it has been noted that the photocurrent (I_{ph}) for devices S5 and S10 have

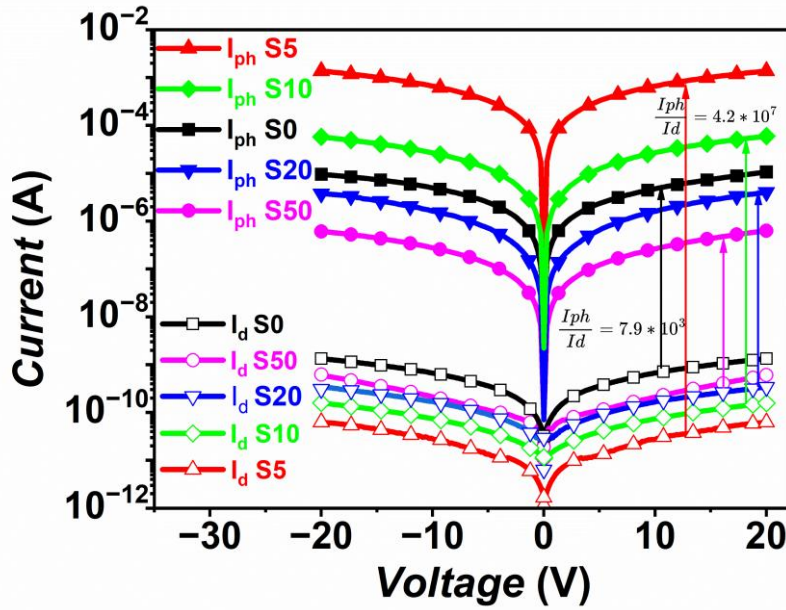


Figure 3.13: Semi-log I-V characteristics of pristine ZnO and Ag-ZnO devices

been increased and the photocurrent for devices S20 and S50 have been decreased accordingly w.r.t pristine ZnO.

Reduction in dark current for all Ag-deposited devices can be attributed to the capture of **thermally excited** electrons from the ZnO conduction band (CB) by Ag-NPs. The Fermi level of silver in bulk form is 4.26 eV, but as the size is reduced to nanoparticle form with silver NPs sizes lying in the range of (0 to 30 nm), the Fermi level of silver is subsequently increased to exceed 5.30 eV [20]. As the Fermi level of unexcited ZnO lies at 5.20 eV, hence for Fermi level alignment Ag-NPs can easily capture the thermally excited electrons from ZnO CB leading to the formation of a depletion zone inside ZnO CB, thereby lowering the dark current for all silver deposited devices (S5, S20, S10, S50).

The increment in photocurrent for smaller silver deposition time-treated devices (S5 & S10) can be attributed to the LSPR effect of silver nanoparticles. Due to the LSPR effect, absorption of UV light is more efficient, especially for the smaller-sized silver nanoparticles [18]. After absorption of UV light, both the d-band's localized electrons (via double photon absorption [21]) and sp-band's delocalized electrons (via single-photon absorption [21]) of Ag-NPs become highly energetic hot electrons due to the transfer of energy to oscillating electrons of Ag-NPs

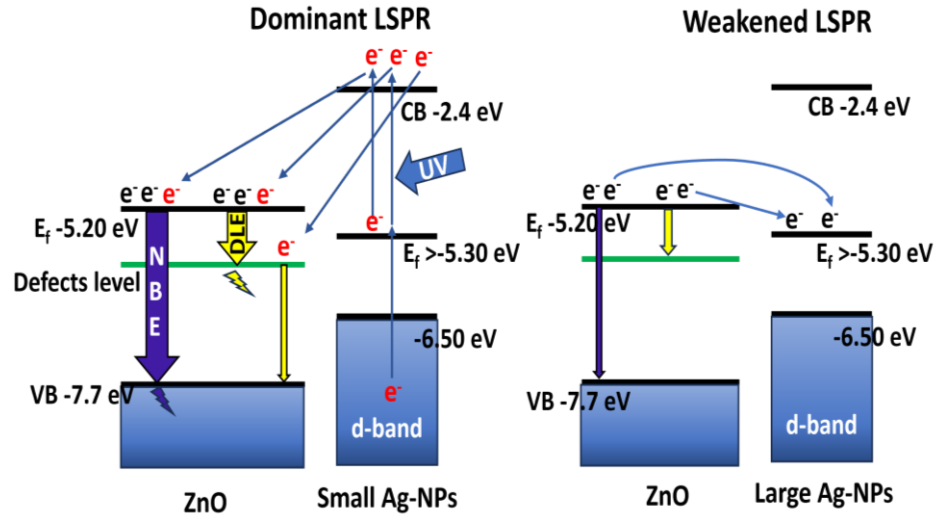


Figure 3.14 Energy level diagram for a) S5 and S10 devices (smaller Ag - NPs based) b) S20 and S50 devices (Larger Ag-NPs based).

from the UV light. These highly energetic hot electrons are excited to the CB of Ag-NPs, shifting the silver nanoparticle's Fermi-level (E_f) to lie near 2.4 eV [21] as shown in Figure 3.14(a). As the new Fermi level of Ag-NPs (~ 2.4 eV) is at a higher level than the UV-excited ZnO Fermi level (~ 5.20 eV), the electrons are transferred from Ag-NPs CB to the ZnO CB for the Fermi level alignment, as shown in Figure 3.14(a). Hence, forming an accumulation region inside the ZnO CB. These increased electron densities inside the conduction band of ZnO will lead to an increment of photocurrent with the applied voltage bias. Furthermore, the increment of photocurrent could also be due to the re-excitation of silver nanoparticle electrons by the defects-related emission of ZnO, which is an energy transfer method instead of a charge transfer method [22]. The significant increase in photocurrent and the reduction in leakage current have greatly enhanced photosensitivity, particularly in the smaller Ag-NPs-based S5 device.

The decrement in photocurrent for larger silver deposition time-treated devices (S20 & S50), can be attributed to the quenching effect by silver nanoparticles. If the size of Ag-NPs increases and becomes comparable to the wavelength of UV light, scattering of UV light may tend to dominate the absorption of UV light [18]. This suppresses the LSPR effect, as the weak absorption of UV light by the Ag-NPs is inadequate to produce hot electrons, owing to an insufficient energy

transfer from the UV light to the oscillating electron. This inhibits the upward shift of the Fermi level, keeping it at (>5.3 eV), as observed under dark conditions, as shown in Figure 3.14(b). As the Fermi level of ZnO (~ 5.20 eV) is higher than the silver Fermi level (>5.3 eV), the photogenerated electrons will be captured by the Ag-NPs, forming the depletion region inside the ZnO CB. This decreased density of electrons inside the conduction band of ZnO leads to the decrement of photocurrent for the (S20 and S50) devices. Although the photocurrent has reduced in the S20 device, the photosensitivity has improved

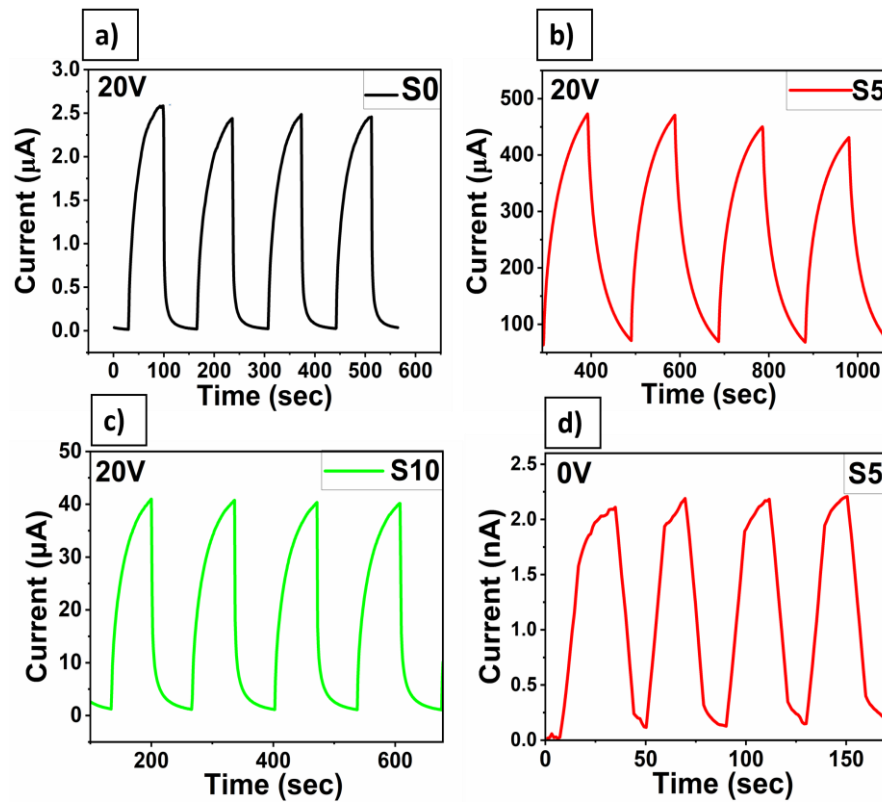


Figure 3.15: Switching Response time graph of a) S0 (pristine ZnO) at 20V bias b) S5 (Ag-ZnO) at 20V bias c) S10 at 20V bias d) S5 at 0V bias devices.

because the dark current of the S20 sample device was significantly reduced.

The switching characteristics of the fabricated UV photodetectors, as shown in Figure 3.15 (a–d), reveal notable differences in transient photoresponse depending on the device structure and applied bias. The pristine ZnO device (S0) under a 20V bias (Figure 3.15a) exhibits a

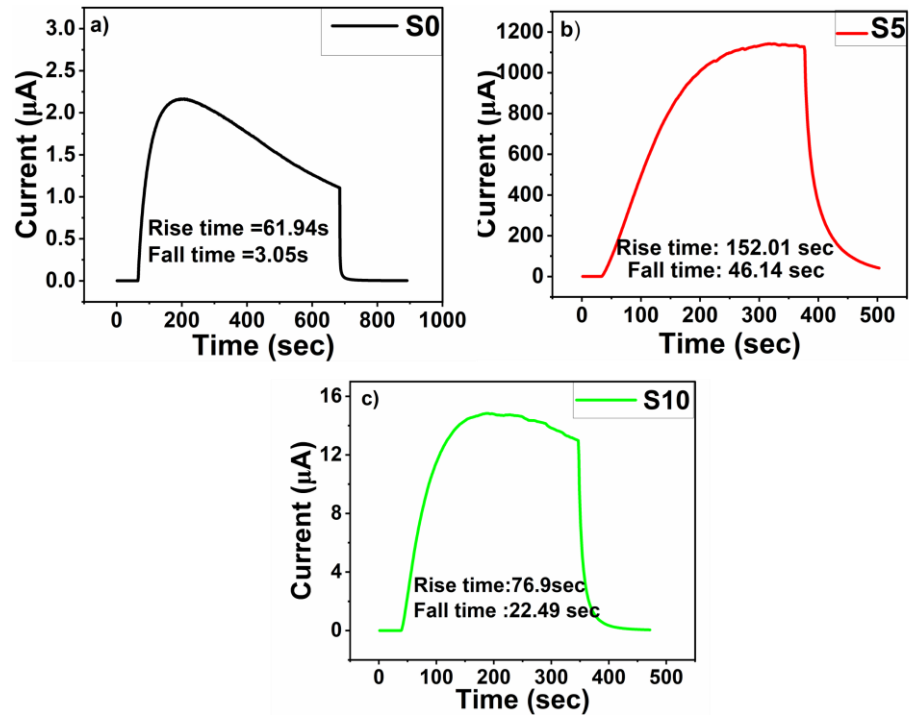


Figure 3.16: Switching Response time graph of a) S5 b) S10 c) S0, with rise time and fall time calculation.

peak photocurrent of approximately 2.8 μA , with a rise time of 61.94 s and a fall time of 3.05 s. This serves as the baseline for comparison.

In contrast, the Ag-decorated ZnO device (S5) under the same 20V bias (Figure 3.15b) demonstrates a significantly higher peak photocurrent of around 500 μA , but with an increased rise and fall time of 152.01 s and 46 s, respectively. Despite the slower switching speed, the photosensitive gain is enhanced by 5316.99 times, indicating a substantial improvement in sensitivity due to the presence of Ag nanoparticles. This enhancement is attributed to the formation of a Schottky junction at the Ag–ZnO interface, which promotes efficient charge separation, suppresses recombination, and facilitates hot electron injection, resulting in higher gain. The S10 device (Figure 3.15c), which likely contains a different Ag concentration or distribution, shows a moderate response with a peak current of $\sim 35 \mu\text{A}$ —improved from S0 but much lower than S5—indicating a trade-off between gain and response speed. Interestingly, the S5 device operated at 0V bias (Figure 3.15d) still exhibits a measurable photocurrent ($\sim 2.5 \text{ nA}$), demonstrating self-powered operation due to the built-in potential of the Schottky junction. This capability is advantageous for low-power applications,

though the photocurrent is significantly reduced compared to biased operation. Overall, these results highlight the critical role of Ag nanoparticle decoration and Schottky junction formation in enhancing photodetector performance, particularly in terms of gain, while also revealing the inherent trade-offs with response time. A bendability test was performed to measure the flexibility of the devices, as shown in

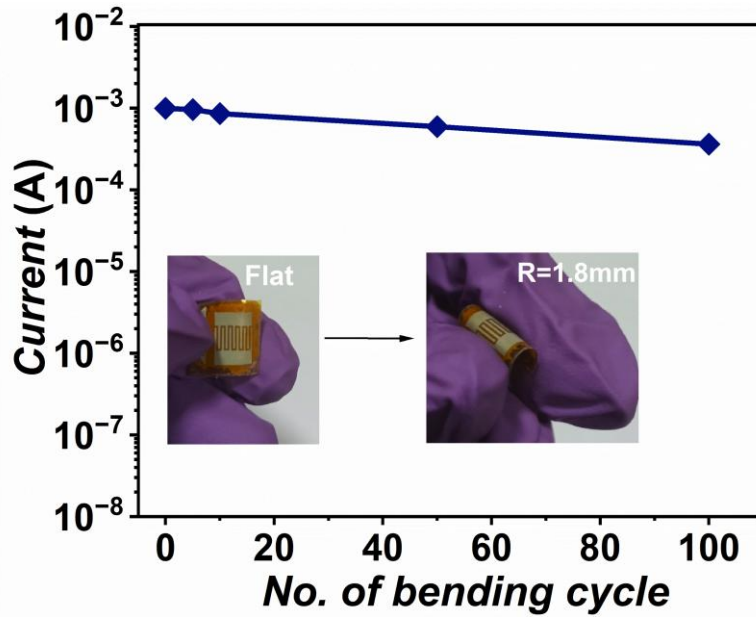


Figure 3.17: Current response vs No. of bending cycle

Figure 3.17. The device was exposed to severe mechanical stress and bending conditions, including a minimum bend radius (R) of 1.8 mm. Further, this bendability test was repeated for up to 100 bending cycles. Our device showed excellent bending stability and photocurrent reproducibility. A gradual reduction in current is observed after 100 cycles, but it remains within 5% of the initial value. This slight decline could be attributed to minor surface fatigue and microcrack formation in the ZnO nanorods or Ag contact interface. However, the retention of over 95% performance demonstrates excellent mechanical stability and flexibility of the polyimide-supported device. This confirms the robustness of the hydrothermally grown ZnO–Ag structure under mechanical stress, making it suitable for wearable electronics.

Table 1 presents the comparison of photosensitivity, responsivity, and specific detectivity across various devices. Table 2 compares the

sensitivity, R_{UV}/R_{Vis} , and responsivity of reported devices with our device.

Table 1: Photosensitivity, Responsivity, and Specific Detectivity of different devices.

Device (@330nm, 0.8mw/cm ² & 20V)	Photo sensitivity (S)	Responsivity (R) (A/W)	Specific Detectivity (D*) (cm·Hz ^{1/2} ·W ⁻¹)	Rise time & fall time (sec)
Pristine ZnO	7.91×10^3	0.2406	2.23×10^{12}	61.94, 3.05
Ag- ZnO_5sec	4.21×10^7	31.17989	2.90×10^{14}	152, 46.14
Ag- ZnO_10sec	3.78×10^5	1.35009	12.56×10^{12}	76.9, 22.49
Ag- ZnO_20sec	1.27×10^4	0.09137	8.30×10^{11}	-
Ag- ZnO_50sec	1.01×10^3	0.01433	1.33×10^{11}	-

Photosensing Mechanism: Under dark conditions, oxygen molecules adsorb on the ZnO surface and extract electrons from the conduction band, creating a surface depletion layer and reducing conductivity. Upon UV illumination, photogenerated holes migrate to the surface and neutralize the adsorbed O_2^- ions, releasing trapped electrons back into the conduction band. In Ag-decorated samples (S5, S10, S20, S50), the presence of silver nanoparticles induces a quenching effect, which efficiently captures thermally generated electrons from the ZnO surface states. This electron trapping by Ag nanoparticles reduces the number of free carriers available in the absence of illumination,

thereby leading to a further decrease in the dark current as shown in Figure 3.18. When exposed to UV light with photon energy exceeding ZnO's bandgap energy, electron & hole pairs are generated inside ZnO NSs. Due to the externally applied electric field, these electron-hole pairs will be separated and the charge carriers will drift to their respective electrodes, thereby increasing the photocurrent. Some of the photogenerated holes will also migrate to the ZnO surface and will release the adsorbed oxygen molecules. This reduces the depletion

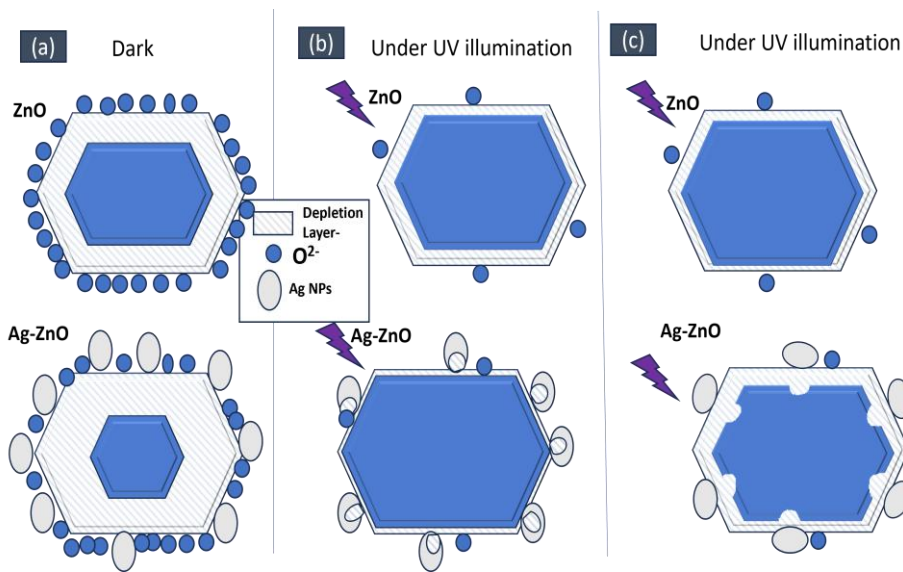


Figure 3.18: Schematic of the depletion region mechanism formation of a) for all the devices in the darkness. b) S5, S10 device under UV light illumination c) for S20, S50 device under UV light illumination

region's width and increases the electron concentration inside pristine ZnO, enhancing photocurrent [10]. However, in Ag-ZnO nanostructures, both oxygen and Ag-NPs contribute to depletion region formation, which depletes the ZnO nanostructures moreover, resulting in a much lower dark current [16]. Further depending on the size of Ag-NPs, the photocurrent in Ag-ZnO NSs may increase due to the plasmonic effect (especially for smaller-sized Ag-NPs) as shown in Figure 3.18 (b) or may decrease due to the quenching effect of silver nanoparticles (for larger-sized Ag-NPs) as shown in Figure 3.18 (c), compared to the pristine ZnO.

Table 2 compares the device performance of this work with Reference 28 [Kumar et al.]. Their ZnO nanorod-based photodetector achieved photosensitivity of ~185 and responsivity of 42.79 A/W under similar UV conditions. In contrast, our optimized S5 sample shows a photosensitivity of 4.2×10^7 and responsivity of 31.79 A/W, demonstrating a significant enhancement. This improvement is due to the synergistic effect of small-sized Ag nanoparticles deposited via the PCR method and optimized hydrothermal ZnO morphology. Moreover, our devices are fabricated on flexible polyimide substrates, enabling bendable configurations, which was not reported in Ref. 28.

Table 2: Comparison of Sensitivity, R_{UV}/R_{vis} , and Responsivity of reported devices with our device

Configuration	λ (nm)	Po (mW/cm ²)	Sensitivity (S)	R_{UV}/R_{vis}	Responsivity (A/W)	References
B-Ga ₂ O ₃	257	-	$\sim 10^2$	$\sim 10^3$	-	[23]
GaN	330	-	1.41×10^4	2.9×10^4	-	[24]
ZnO-Al	300	1201	-	-	42.5	[25]
ZnO-Pd	400	40	22.65	-	0.01	[26]
ZnO/Au/ZnO	315	-	350	1.32×10^3	10.64	[27]
Ag-ZnO (IDE)	395	1.5	185	-	42.79	[28]
Ag-ZnO (MSM)	365	4000	1913	-	1.01	[29]

Configurati on	λ (nm)	Po (mW/c m²)	Sensitivity (S)	R_{UV}/R_{vis}	Responsi vity (A/W)	Refer ences
ZnO (IDE)	330	0.8	1.27×10⁴	3.23×10³	0.24	This work
Ag-ZnO (IDE)	330	0.8	4.21×10⁷	1.75×10⁴	31.79	

Chapter 4

Conclusions and Future Scope

4.1 Conclusions:

We successfully have grown highly oriented, crystalline, densely packed, and homogeneous ZnO nanorods on a polyimide substrate and also successfully fabricated the completely solution-processed Ag-ZnO nanostructures towards the development of highly sensitive, UV-A selective, responsive, and stable UV photodetector. Further solution-processed Ag-ZnO nanostructures have shown good adhesion with the polyimide substrate which has enhanced the flexibility of the device. The adhesion quality verification was conducted using two primary tests: (i) a mechanical bending test over 100 cycles, and (ii) a tape-peel test using standard Scotch tape applied and removed repeatedly over the nanostructure area. The increased surface area provided by the nanorods and the plasmonic effects of silver nanoparticles enhances the UV absorption and promote efficient charge carrier dynamics. By suitably controlling the UV illumination time, the plasmonic effects of different sizes of silver nanoparticles have been studied intensively. The optimal deposition time of 5 seconds for silver nanoparticles results in the best device performance. As compared to pristine ZnO, the Ag-deposited ZnO (i.e. S5 device) significantly suppresses leakage current from 1.23×10^{-9} A to 3.05×10^{-11} A and increases photocurrent from 1.05×10^{-5} A to 1.37×10^{-3} A. Photosensitivity has been increased from 7.918×10^3 to 4.21×10^7 against a $\lambda = 330$ nm UV light illumination and bias of 20 V. Furthermore, the UV to visible rejection ratio ($R_{(330\text{nm})}/R_{(450\text{ nm})}$) has

been raised from 3.008×10^3 to 1.75×10^4 and the Responsivity has been raised from 0.2406 to 31.17 A/W. The improved performance of the photodetector under mechanical bending tests confirms the suitability of the flexible polyimide substrate, emphasizing the potential of this device structure in wearable electronics. This work demonstrated the potential of effective plasmonic coupling between Ag-NPs and ZnO NRs and its effective utilization towards the development of highly sensitive UV photodetector and also highlights the potential of this effective solution processed-based technique in the development of highly sensitive, air-stable, flexible UV photodetectors. The results indicate the potential application of these flexible devices in environmental monitoring and space exploration where high sensitivity to UV light is critical.

4.2 Future scope

In this work, we have presented a high-sensitivity UV photodetector featuring Ag nanoparticles, which were photochemically deposited onto hydrothermally synthesized ZnO nanostructures on a polyimide substrate. The resulting Ag-ZnO nanostructures show promise as a cost-effective solution for creating highly photosensitive and stable devices suitable for a wide range of commercial applications. The exploration of other metal nanoparticles for similar enhancements could further broaden the applications of this technology by incorporating alternative metal nanoparticles such as gold, aluminum or platinum, the optical and electrical properties of the photodetectors could be further optimized. Additionally, integrating advanced materials like graphene or MoS₂ might expand the device's detection range beyond UV into visible or even infrared light, making it suitable for broader applications in imaging, spectroscopy, and remote sensing. The time of switching response of the fabricated device is measured in seconds, so it cannot be used for certain applications where high response speed is required. The response speed can be further increased by incorporating an additional layer of p-type semiconductor material, such as organic semiconductors, to improve charge separation.

Moreover, the as-fabricated S50 device could potentially be used for photocatalytic applications due to its enhanced separation of photo-generated excitons at the Ag–ZnO interface. In this structure, organic molecules can be efficiently degraded by capturing electrons from the silver nanoparticle surface. In contrast, in the S5 device, the electron capture is likely to occur from the ZnO surface instead, indicating a reversal in the charge carrier extraction pathway.

References

Chapter (3 & 4)

- [1] X. Xia, J. Tu, Y. Zhang, X. Wang, C. Gu, X. B. Zhao, and H. J. Fan, "High-quality metal oxide core/shell nanowire arrays on conductive substrates for electrochemical energy storage," *ACS Nano*, vol. 6, no. 6, pp. 5531, 2012, doi: 10.1021/nm301454q
- [2] L. Dai, W. C. Cheong, C. H. Sow, C. T. Lim, and V. B. Tan, "Molecular dynamics simulation of ZnO nanowires: size effects, defects, and super ductility," *Langmuir*, vol. 26, no. 2, pp. 1165-1171, 2010, doi: 10.1021/la9022739.
- [3] Y. Duan, X. Liu, L. Han, S. Asahina, D. Xu, Y. Cao, Y. Yao, and S. Che, "Optically active chiral CuO nanoflowers," *Journal of the American Chemical Society*,
- [4] M. J. Zheng, L. D. Zhang, G. H. Li, X. Y. Zhang, and X. F. Wang, "Ordered indium-oxide nanowire arrays and their photoluminescence properties," *Applied Physics Letters*, vol. 79, no. 6, pp. 839, 2001, doi: 10.1063/1.1389071.
- [5] A. B. Sushkov, O. Tchernyshyov, W. Ratcliff, S. W. Cheong, and H. D. Drew, "Probing spin correlations with phonons in the strongly frustrated magnet ZnCr_2O_4 ," *Physical Review Letters*, vol. 94, no. 13, 137202, 2005, doi: 10.1103/PhysRevLett.94.137202.
vol. 136, no. 20, pp. 7193–7196, 2014, doi: 10.1021/ja500197e.
- [6] W. Tian, C. Zhang, T. Zhai, S.-L. Li, X. Wang, M. Liao, K. Tsukagoshi, D. Golberg, and Y. Bando, "Flexible SnO_2 hollow nanosphere film based high-performance ultraviolet photodetector," *Chemical Communications*, vol. 49, no.36,pp.3739,2013,doi:10.1039/C3CC39273B.
- [7] J.F. Muth, R.M. Kolbas, A.K. Sharma, S. Oktyabrsky, J. Narayan (1999), Excitonic structure and absorption coefficient measurements of ZnO single crystal epitaxial films deposited by pulsed laser deposition, *J. Appl. Phys.*, 85 (11),7884-7887(doi:http://dx.doi.org/10.1063/1.370601).
- [8] P.F. Carcia, R.S. McLean, M.H. Reilly, G. Nunes (2003), Transparent ZnO thin-film transistor fabricated by RF magnetron sputtering, *Appl. Phys. Lett.*, 82 (7),1117-1119(doi:http://dx.doi.org/10.1063/1.1553997).
- [9] H. Wan, H.E. Ruda (2010), A study of the growth mechanism of CVD-grown ZnO nanowires, *J. Mater. Sci.: Mater. Electron.*, 21 (10), 1014-1019 (doi:http://dx.doi.org/10.1007/s10854-010-0118-7).

- [10] T. Dixit, A. Bilgaiyan, I.A. Palani, D. Nakamura, T. Okada, V. Singh (2015), Influence of potassium permanganate on the anisotropic growth and enhanced UV emission of ZnO nanostructures using hydrothermal process for optoelectronic applications, *J. Sol-Gel Sci. Techn.*, 75 (3), 693-702 (doi: <http://dx.doi.org/10.1007/s10971-015-3741-1>).
- [11] M. Kim, T. Park, S. H. Kim, and S. Kim, "Low-temperature large-area fabrication of ZnO nanowires on flexible plastic substrates by solution-processible metal-seeded hydrothermal growth," *Nano Convergence*, vol. 7, no. 36, pp. 1-10, 2020, doi: 10.1186/s40580-020-00235-6.
- [12] S. Singh, M. Kumar, and J. Kumar, "ZnO nanostructures fabricated using thermal evaporation: Growth and properties," *J. Mater. Sci. Mater. Electron.*, vol. 28, no. 18, pp. 13537–13544, 2017. DOI: 10.1007/s10854-017-7230-6.
- [13] S. Jeong, J. H. Kim, and S. Cho, "ZnO nanostructure formation on sputtered metal substrates for optoelectronic applications," *Appl. Phys. Lett.*, vol. 109, no. 6, pp. 063107, 2016. DOI: 10.1063/1.4960911.
- [14] P. Das, N. Chakraborty, and S. Sen, "Synthesis of ZnO nanostructures using solution processing techniques for enhanced photocatalytic activity," *J. Nanomater.*, vol. 2018, Article ID 8571234, 2018. DOI: 10.1155/2018/8571234.
- [15] J. Agrawal, T. Dixit, A. I. Palani, M. S. R. Rao, and V. Singh, "Zinc interstitial rich ZnO honeycomb nanostructures for deep UV photodetection," *Phys. Status Solidi (RRL) Rapid Res. Lett.*, vol. 12, no. 10, Oct. 2018, Art. no. 180024
- [16] A. Yadav, J. Agrawal, and V. Singh, "Development of visible-blind UV photodetector using solution-processed Ag-ZnO nanostructures," *IEEE Photon. Technol. Lett.*, vol. 33, no. 19, pp. 1065–1068, Oct. 1, 2021, doi: 10.1109/LPT.2021.3103097.
- [17] S. J. Young and L. T. Lai, "UV illumination and Au nanoparticles enhanced ZnO nanorods field electron emission device," *IEEE Transactions on Electron Devices*, vol. 67, no. 1, pp. 304–308, Jan. 2020, doi:10.1109/TED.2019.2946931.
- [18] B. Mekuye, "The Impact of Size on the Optical Properties of Silver Nanoparticles Based on Dielectric Function," *IntechOpen*, submitted June 8, 2023, reviewed Nov. 22, 2023, and published Dec. 28, 2023. DOI: 10.5772/intechopen.113976.
- [19] P. K. Jain, K. S. Lee, I. H. El-Sayed, and M. A. El-Sayed, "Calculated absorption and scattering properties of gold nanoparticles of different size, shape, and composition: applications in biological imaging and biomedicine," *The Journal of Physical Chemistry B*, vol. 110, no. 14, pp. 7238-7248, 2006, doi:10.1021/jp057170o.
- [20] Y. Noh, J. Shin, H. Lee, G. Y. Kim, M. Kumar, and D. Lee, "Decoration of Ag nanoparticle on ZnO nanowire by intense pulsed light and enhanced UV

- photodetector," *Chemosensors*, vol. 9, no. 11, 2021, doi: 10.3390/chemosensors9110321.
- [21] H. H. Mai et al., "Nonlinear optical properties of Ag nanoclusters and nanoparticles dispersed in a glass host," *The Journal of Physical Chemistry C*, vol. 118, no. 29, pp. 15995-16002, 2014, doi: 10.1021/jp502294u.
- [22] T. Dixit, J. Agrawal, S. V. Solanke, K. L. Ganapathi, M. S. R. Rao, and V. Singh, "ZnO/Au/ZnO configuration for high-performance multiband UV photo-detection," *IEEE Sensors Letters*, vol. 3, no. 9, pp. 1-4, 2019, doi: 10.1109/lens.2019.2940764.
- [23] A. S. Pratiyush et al., "Optical float-zone grown bulk β -Ga₂O₃-based linear MSM array of UV-C photodetectors," *IEEE Photonics Technology Letters*, vol. 31, no. 12, pp. 923-926, Jun. 15, 2019. doi: 10.1109/LPT.2019.2913286.
- [24] M. Garg, B. R. Tak, V. R. Rao, and R. Singh, "Enhanced performance of MSM UV photodetectors by molecular modification of gallium nitride using porphyrin organic molecules," *IEEE Transactions on Electron Devices*, vol. 66, no. 4, pp. 1761-1766, Apr. 2019. doi: 10.1109/TED.2019.2901022.
- [25] M. T. Khan, K. H. Prasad, A. Khan, and M. Shkir, "Enhancement of photodetector performance of aluminum-doped zinc oxide thin films fabricated via SILAR method: Structural, optical, and electrical analysis," *Inorganic Chemistry Communications*, vol. 169, p. 112973, Aug. 2024. doi: 10.1016/j.inoche.2024.112973.
- [26] K. L. Karthikeyan, A. M. V. Akshaya, and P. K. Basu, "Microwave-assisted synthesis of ZnO and Pd-ZnO nanospheres for UV photodetector," *Sensors and Actuators A: Physical*, vol. 263, pp. 416-423, Jul. 2017, doi: 10.1016/j.sna.2017.06.013.
- [27] T. Dixit, J. Agrawal, S. V. Solanke, K. L. Ganapathi, M. S. Ramachandra Rao, and V. Singh, "ZnO/Au/ZnO Configuration for High Performance Multiband UV Photo-Detection," *Electromagnetic Wave Sensors*, vol. 3, no. 9, p. 3501604, Sept. 2019, doi: 10.1109/LESENS.2019.2940764.
- [28] S. M. Mohammad, S. Rajamanickam, Z. Hassan, M. Abdullah, A. R. Shafiq, and A. Abuelsamen, "Self-powered UV photodetector performance optimization based on Ag nanoparticles-encapsulated-ZnO nanorods by photo-deposition method," *Sensors and Actuators A: Physical*, vol. 332, p. 113032, Aug. 2021, doi: 10.1016/j.sna.2021.113032.
- [29] Y.-L. Chu, S.-J. Young, Y.-J. Chu, Y.-H. Liu, and T.-T. Chu, "High-performance UV photodetectors based on 1-D Ag/ZnO nanostructures with a simple photochemical process at room temperature," *IEEE Electron Device Letters*, vol. 44, no. 1, pp. 124-127, 2023, doi: 10.1109/led.2022.3220753.

List of Publications

Conference Participation:

N. Nikhil and V. Singh*, “*Silver Nanoparticle Decorated ZnO Nanorod Array Based Highly Sensitive Photodetector*”, 34th Annual Meeting of the Materials Research Society of Japan (MRS-J), [2024].

Journal Publication:

Development of Silver Nanoparticle-Decorated ZnO Nanorod Array-Based Highly Sensitive Photodetector.

Manuscript Status: Submitted to *Journal of Materials Science: Materials in Electronics* (Springer). Currently under peer review – reviewer comments received and under revision

Authors: N. Nikhil, J. Agrawal, and V. Singh*

Patent manuscript under preparation:

All solutions processed Flexible UV Photodetector.

Authors: N. Nikhil, and V. Singh.